

1           **BB-SPEEDset: a validated dataset of broadband near-source**  
2           **earthquake ground motions from 3D physics-based numerical**  
3                           **simulations**

4  
5                           by Roberto Paolucci, Chiara Smerzini, Manuela Vanini

6  
7  
8  
9  
10                           **Corresponding Author**

11   Chiara Smerzini

12   Department of Civil and Environmental Engineering, Politecnico di Milano

13   Piazza Leonardo da Vinci, 32 – 20133 Milano, Italy.

14   E-mail: [chiara.smerzini@polimi.it](mailto:chiara.smerzini@polimi.it)

15  
16  
17                           **Declaration of Competing Interests**

18  
19   The authors acknowledge there are no conflicts of interest recorded.

20

21

## Abstract

22 This paper provides an overview of the BB-SPEEDset, a strong-motion dataset of near-source  
23 broadband earthquake ground motions from 3D physics-based numerical simulations, obtained by  
24 the spectral element code SPEED developed at Politecnico di Milano, Italy. Taking advantage of  
25 the earthquake ground motion scenarios produced so far by SPEED, in most cases validated against  
26 earthquake recordings, the main objective of this work is to construct and validate a dataset of  
27 simulated broadband waveforms to be used as a support for characterization and modelling of  
28 near-source earthquake ground motions. To pursue this objective, the following steps were  
29 necessary, namely: (i) the implementation of an effective workflow suitable to process in an  
30 homogeneous format various SPEED simulations; (ii) the generation of broadband time histories  
31 using a technique based on Artificial Neural Networks, trained on strong motion records; (iii) the  
32 creation of a flat-file collecting, for each simulated scenario, the most relevant metadata (fault  
33 rupture scenario, site response proxies, source-to-site distances) as well as a comprehensive set of  
34 ground motion intensity measures of the processed broadband waveforms (Peak Ground  
35 Acceleration, Velocity and Displacement, spectral ordinates, duration, pulse period, etc.). Finally,  
36 a comprehensive set of consistency checks is made to verify the absence of any systematic bias in  
37 the trend of the BB-SPEEDset results with respect to the NESS v2.0 near-source recorded ground  
38 motion dataset. Indeed, the main features of near-source ground motion in BB-SPEEDset, ranging  
39 from the statistical distributions of peak and integral measures both at short and long periods, the  
40 ground motion attenuation with distance, to the features of impulsive ground motions and  
41 directionality effects, are in substantial agreement with those from NESS.

## 42 **Keywords**

43 earthquake ground motions, near-source conditions, 3D physics-based numerical simulations,

44 simulated broadband waveforms dataset.

## Introduction

45

46 It is well known that the characterization of earthquake ground motion in the near-source region  
47 is made difficult by the paucity of records that, in spite of their ever-growing number, cannot  
48 reliably describe yet neither the median values nor their variability, in the variety of source and  
49 site conditions typically present in the vicinity of the seismogenic fault.

50 As in most fields of science, when the laboratory investigations are either limited or prevented  
51 owing to the size of the prototype and to the difficulties to reproduce the in-field conditions,  
52 analytical and numerical modelling may be an alternative to complement in an ideal laboratory the  
53 information that is difficult to capture from nature.

54 In this perspective, the so-called physics-based numerical simulations (PBS) of earthquake ground  
55 motion aim at complementing the recorded data by providing simulated results in the source and  
56 site configurations that may resemble as closely as possible the real ones. In some cases, the role  
57 of PBS has been extended to provide realistic seismic scenarios of earthquake ground motions  
58 suitable to improve the approaches for seismic hazard and risk analysis (see e.g., Graves et al.  
59 2011, Maeda et al. 2016, Smerzini and Pitilakis 2018, Bradley et al. 2017 and 2020, Stupazzini et  
60 al. 2021) and to provide input for seismic structural analyses (Galasso et al. 2013, Baker et al.  
61 2021, Fayaz et al., 2021).

62 With this objective, several research groups worldwide (see e.g., amongst others, Graves and  
63 Pitarka 2010 and 2015; Irikura and Miyake 2011; Mazzieri et al. 2013; Komatitsch et al. 2013;  
64 Isbilibiroglu et al. 2015; Paolucci et al. 2018; Lu et al. 2018; McCallen et al. 2020a and 2020b) have  
65 continuously contributed in the recent years to development of numerical tools that may become  
66 more and more suitable to produce, with a reasonable computational effort, realistic earthquake  
67 ground motions that may reliably complement the recorded ones in the near-source region and

68 eventually coupled with engineering models for non-linear structural response.

69 Combining the computational burden with the difficulty to accurately reproduce details of the fault  
70 geometry, of the seismic slip distribution, and of the complex geology (typically 3D) of the area  
71 of interest, that may extend by tens of km, PBS are generally considered to be bounded within  
72 frequency limits hardly beyond about 2-3 Hz, although some successful examples of PBS  
73 extending up to 8-10 Hz in the presence of very detailed knowledge of local site conditions are  
74 also present, such as for the simulation of induced seismicity in the Groningen (Netherlands) area  
75 (Paolucci et al., 2021).

76 Some cross-verification activities of numerical tools for PBS were undertaken in the recent past  
77 (Chaljub et al. 2010; Bielak et al. 2010; Maufroy et al. 2015), that were seminal steps for the  
78 different research groups to solve the major issues arising when the numerical codes are applied  
79 to very complex configurations. However, relatively little effort was devoted up to now to  
80 comprehensive validations of PBS against strong motion records, especially in the near-source  
81 region (Taborda and Bielak 2013 and 2014, Paolucci et al. 2015, Imperatori and Gallovič 2017,  
82 Gatti et al. 2018, Pitarka et al. 2020, Paolucci et al. 2021). For this reason, a blind prediction  
83 experiment was set up in the framework of the 6th IASPEI/IAEE International Symposium - The  
84 Effects of Surface Geology on Seismic Motion (ESG6), with the objective to reproduce earthquake  
85 ground motions during the Kumamoto, Japan, seismic sequence of 2016, with a moment  
86 magnitude  $M_w$  7 mainshock.

87 With a long-lasting expertise gained (i) in the development of the open-source numerical code  
88 SPEED based on spectral elements (Mazzieri et al. 2013), (ii) in the advancement of techniques to  
89 enrich at high frequencies the PBS results (Paolucci et al. 2018), (iii) in the validation of PBS  
90 results against near-source ground motions recorded from different earthquakes in Italy and

91 worldwide and in the application to several scenario case studies (see overview in Table 1), we  
92 have collected a large subset of our simulated results with a uniform processing procedure that will  
93 be illustrated in the sequel. In this way, we have constructed the BB-SPEEDset (v1.0), a dataset  
94 of broadband near-source ground motions aiming at providing a complementary tool for  
95 characterization of earthquake ground motions, in terms of their dependency on magnitude,  
96 distance and site conditions, such as the most common empirical ground motion models (GMM),  
97 with a complete and well constrained characterization in terms of seismic source and site  
98 conditions. Additionally, this dataset may also provide the basis to properly analyze the spatial  
99 variability of ground motion, with potential important implications to validate and improve the  
100 existing models for spatial correlation (e.g., Infantino et al., 2021b; Schiappapietra and Smerzini,  
101 2021) and spatial coherency, that currently suffer from the lack of records from sufficiently densely  
102 spaced arrays of seismic stations (e.g. Smerzini 2018).

103 As introduced by D’Amico et al. (2017), the main advantage of a broadband ground motion dataset  
104 based on PBS is that all input source data are clearly identified, as well as the site conditions of  
105 recording stations, and ground shaking scenarios of the simulated earthquakes can easily be  
106 constructed. On the other side, it is difficult to prove that the available waveforms are not biased  
107 with respect to records, in terms of the different parameters of ground motion that are relevant for  
108 engineering applications, typically because of the limited detail of the input data of PBS in terms  
109 of seismic source and geological layering, and because of the computational limits of the numerical  
110 simulations.

111 To overcome such limitations, the novelty of this paper is to provide a comprehensive comparison  
112 of the BB-SPEEDset statistical distributions with those obtained by NESS2.0 (denoted in the  
113 following by NESS), a dataset of worldwide recorded near-source ground motions addressed in

114 this special issue by Sgobba et al. (2021), updated after Pacor et al. (2018). Although the origin of  
115 the two datasets is completely different, BB-SPEEDset being based on relatively few earthquake  
116 scenarios, each with a large sample of simulated accelerograms, while NESS is based on a large  
117 number of real earthquakes, each with relatively few records, such comparison is a crucial step to  
118 assess whether a bias exists between the trend of simulated results in the BB-SPEEDset with  
119 respect to those of NESS. The absence of systematic differences will strongly support the  
120 effectiveness of the procedure to produce broadband waveforms from the SPEED physics-based  
121 numerical simulations as well as the potential use of the BB-SPEEDset to improve the available  
122 tools for the prediction of near-source earthquake ground motion and to provide input motions for  
123 earthquake engineering analyses.

124 This paper is organized as follows. After an introduction of the workflow for post-processing PBS  
125 results and for generating broadband waveforms by taking advantage of Artificial Neural  
126 Networks (ANN), the BB-SPEEDset is introduced with its current features, in terms of distribution  
127 of simulated waveforms according to magnitude, distance, site conditions. Subsequently, a  
128 comprehensive comparison of the BB-SPEEDset trends with respect to those of the NESS dataset  
129 is presented, involving the statistical distribution of various IMs, their attenuation with distance,  
130 and the main features of near-source ground motion such as directionality, vertical components  
131 and impulsive motions. Finally, an example of a query by earthquake scenario from the BB-  
132 SEEDset is introduced with reference to the 2009 L'Aquila earthquake, where one of the main  
133 advantages of a dataset based on PBS can be appreciated, in terms of generation of ground motion  
134 maps of a selected earthquake scenario.

135

136

137

## Workflow for post-processing of SPEED results

138 A fundamental step for the construction of a database of PBS results is the definition of an  
139 optimized workflow for post-processing of results of SPEED simulations in a uniform and  
140 repeatable format. To this end, the SPEED kernel is supplemented by a set of Matlab routine  
141 packages that allow to post-process the raw waveforms computed by SPEED (typically,  
142 displacement time histories at receiver points) and generate outputs and metadata in a standard  
143 format. Note that, for the earthquake scenarios included in BB-SPEEDset, kinematic rupture  
144 models were introduced, consisting of heterogeneous slip functions across the fault. While for real  
145 earthquakes (validations in Tab. 1) the kinematic source parameters were calibrated based on the  
146 available seismic source inversions studies, for ideal scenario earthquakes the kinematic rupture  
147 generators proposed by Herrero and Bernard (1994) and Schmedes et al. (2012) are adopted. The  
148 generation of these fault slip distributions is handled by means of specific Matlab routines,  
149 implemented in the pre-processing tools of SPEED.

150 An overview of the post processing workflow is given in Figure 1 and it is organized in the  
151 following steps:

- 152 • *3PTOOL*: the code extracts and organizes the raw SPEED seismograms in a common  
153 format (output file: Matlab .mat file) including receiver coordinates, displacement time  
154 histories (unfiltered), low frequency (directly from SPEED) and broadband (from  
155 ANN2BB, see following Section) peak ground motion maps.
- 156 • *SITE RESPONSE PROXIES*: the routine computes from the velocity model the most  
157 relevant site response proxies, namely:  $H_{bed}$  – depth of the alluvial-bedrock interface  
158 included in the simulation model,  $H_{800}$  – depth at which the shear-wave velocity  $V_s$  is equal  
159 or higher than 800 m/s,  $V_{S30}$  – time averaged shear-wave velocity from the surface to a



160 depth of 30 meters,  $V_{Seq}$  – time averaged shear-wave velocity from the surface to  $H_{800}$  (if  
161  $H_{800} \leq 30$  m; if  $H_{800} > 30$  m, then  $H_{800} = 30$ m), see definition in the Italian Building Code  
162 (NTC 2018),  $V_{Sbed}$  – time averaged shear-wave velocity from the surface to  $H_{bed}$ ,  $V_{S800}$  –  
163 time averaged shear-wave velocity from the surface to  $H_{800}$ ; topography slope.

164 • *EFFECTIVE FAULT*: the code calculates the effective dimensions of the rupture fault area  
165 according to the procedure originally proposed by Mai and Beroza (2000), and extended  
166 by Thingbaijam and Mai (2016), see Figure 2. This step is particularly relevant to define  
167 metadata with unbiased source dimensions, as the fault implemented in the numerical grid  
168 (typically, the fault associated with a maximum magnitude to be simulated) may be  
169 different from the co-seismic rupture area associated with a given earthquake scenario.  
170 Effective source dimensions are based on the definition of autocorrelation width  
171 (Bracewell, 1986) of slip distributions, calculated in along-strike and down-dip directions.  
172 These slip functions are computed summing up the slip in columns (or rows) on the  
173 rectangular rupture plane. An iterative, trimming, process determines the largest  
174 dimensions that fit the autocorrelation width, according to the subfault size. The  
175 dependence of these effective measures on magnitude through scaling relationships has  
176 been verified (using e.g. Wells and Coppersmith 1994 or Leonard 2010).

177 • *SELECT RECEIVERS*: the code extracts subsets of receiver points according to prescribed  
178 sampling techniques. Since the simulated seismograms are generally obtained at tens of  
179 thousands of receivers, the computation of broadband time histories and of all  
180 corresponding intensity measures is limited to a subset of receivers to minimize the  
181 computational cost. In our processing for the BB-SPEEDset, the receiver selection was  
182 defined to achieve a higher density of receivers at lower distances from the source.

- 183       • *BROADBAND GENERATION*: at the selected receivers, the SPEED signals (typically  
184       reliable up to about 1.5-2 Hz, see Table 1) are enriched at high frequencies using a  
185       technique based on ANN trained on strong ground motion recordings (referred to as  
186       ANN2BB).
- 187       • *SPEED IDCards*: the routine produces an informative sheet (.pdf) summarizing the main  
188       features of the numerical model (e.g. mesh, wave velocity model), of the simulated fault  
189       rupture scenario (e.g. fault slip distribution, rise time, rupture times, etc..) and a selection  
190       of outputs (e.g. ground shaking maps).
- 191       • *FLAT-FILE GENERATION*: a flat-file is created in a format consistent with the one  
192       adopted in up-to-date strong motion databases (e.g. NESS) and populated with an  
193       exhaustive list of metadata (regarding the source, source-to-site distances, site response  
194       proxies, post-processing, etc..) and ground motion IMs.

195

196

### **Broadband generation**

197   As well known, the accuracy of the PBS is limited to the long period range  $T \geq T^*$ , with  $T^*$  being  
198   typically in the range of 0.5 - 1 s (see maximum frequency in Table 1), mainly due to the lack of  
199   knowledge about the Earth crust and earthquake rupture process at short-wavelength and partially  
200   due to the computational cost of large and fine grids. For this reason, the core of the post-  
201   processing workflow is the generation of broadband waveforms, where the low-frequency  
202   simulated waveforms are enriched in the high-frequency range to produce time histories with a  
203   realistically broad frequency content. This is an essential step to treat the simulated waveforms in  
204   the same way as recordings and, therefore, make them usable in earthquake engineering  
205   applications.

206 To this end, the ANN2BB approach (Paolucci et al. 2018), based on Artificial Neural Networks  
207 trained on strong ground motion recordings, is adopted. In this work, the ANN2BB technique has  
208 been enhanced with respect to the original version published in 2018 to make it suitable for massive  
209 post-processing of larger datasets in a semi-automated fashion and to improve the quality of  
210 generated waveforms.

211 Referring to Paolucci et al. (2018) for further details, the ANN2BB procedure is based on four  
212 main steps, as sketched in Figure 3:

213 (1) An ANN, consisting of two-layer feed-forward neural network with 30 hidden neurons, is  
214 trained on a dataset of strong motion records, such as SIMBAD v6 (Smerzini et al. 2014)  
215 or NGA-West 2 (Ancheta et al. 2013), to predict short period spectral ordinates ( $T < T^*$ )  
216 based on the long period ones ( $T \geq T^*$ ). Different ANNs are trained separately on the  
217 geometric mean of the horizontal components and on the vertical components for  
218 prediction of three-component ground motions.

219 (2) For each simulated waveform, a target ANN2BB response spectrum is computed, the long  
220 spectral ordinates of which, for  $T \geq T^*$ , coincide with the simulated ones, while, for  $T < T^*$ ,  
221 they are obtained from the ANN (separately for horizontal and vertical components). In  
222 our application, the corner period  $T^*$  is set depending on the frequency-limitation of the  
223 numerical mesh. To preserve variability of the ANN results, the target at short periods is  
224 built on the median value calculated over 20 ANN realizations.

225 (3) Once the ANN2BB target spectrum is defined for each waveform, the non-stationary  
226 stochastic approach by Sabetta and Pugliese (1996) is followed to generate the high  
227 frequency portion of the signal. Updates of this approach (see e.g. Pousse et al., 2006;  
228 Sabetta et al. 2021) will be implemented in the next releases of the BB-SPEEDset. More

229 specifically, 20 stochastic realizations are obtained, according to the simulated scenario  
 230 ( $M_w$ ) and receiver (distance, site conditions) and, out of these, a specific realization is  
 231 selected based on the criteria illustrated in the sequel.

232 (4) The selected stochastic signal (HF) and the PBS waveform (LF), previously filtered in the  
 233 high and low frequency range, respectively, are combined in the time domain. Phase  
 234 matching between HF and LF is achieved by alignment of the two time histories according  
 235 to the instant at 5% of normalized Arias intensity.

236 The scaling and selection of the stochastic signal of step (3) is based on a two-step procedure of  
 237 minimization of the residuals with respect to the target ANN2BB spectrum. First, for each  
 238 stochastic realization, a scaling factor  $SF$  that minimizes the residuals with respect to the target is  
 239 calculated and, subsequently, among the different scaled stochastic signal the one with the  
 240 minimum misfit is selected. The residuals are computed using the following equation:

$$241 \quad \min_{nsim} r^{nsim} = \min_{nsim} \left( \min_{SF} \sum_{i=1}^{N_{periods}} w_i \left( \frac{\ln ANN_{median,i} - \ln(SF * STOCH_i^{nsim})}{\sigma_{\ln ANN,i}} \right)^2 \right) \quad (1)$$

242 where  $SF$  is the scaling factor (typically in the range 0.5-2),  $N_{periods}$  are the vibration periods of  
 243 the target ANN spectrum,  $w_i$  is the weight-vector,  $nsim = 20$  is the total number of stochastic  
 244 signal realizations (20 realizations are found to guarantee a satisfying final spectrum).  $STOCH^{nsim}$   
 245 is the  $nsim^{th}$  stochastic realization. Note that both median ( $ANN_{median}$ ) and standard deviation  
 246 ( $\sigma_{\ln ANN}$ ) of the 20 ANN are used to calculate the misfit. The weight-vector  $w$  controls the fit to the  
 247 target ANN spectrum. As the fit is actually performed only on the HF range, the weight vector  
 248 takes the following values:  $w = 0$  for  $T > T^*$ ;  $w = 1$  for  $T < T^*$  and  $w = 2$  for  $T = T^*$ . These values  
 249 were selected after appropriate sensitivity analyses and they ensure that at the end of the procedure,  
 250 the final spectrum is ‘as close as possible’ to the PBS one in the LF range, including the merging

251 period.

252 The main differences with respect to the procedure introduced by Paolucci et al. (2018) are the  
253 following:

254 - step 2: the target ANN2BB in the high frequency range is computed as the median of 20 different  
255 ANN realizations, rather than the output of a single ANN, in order to achieve a greater stability of  
256 results and minimize overfitting issues;

257 - step 3: the frequency scaling of the stochastic signal is replaced by a linear scaling in the time  
258 domain to approach the target ANN2BB spectrum at short periods. This improvement overcomes  
259 some issues related to the unrealistic frequency content, that was sometimes introduced by the  
260 manipulation of Fourier spectra in the previous procedure. Furthermore, owing to its  
261 computational efficiency, it makes the broadband generation tool of SPEED suitable for massive  
262 computations over a very large number of receivers with no manual interventions, facilitating time-  
263 effective yet reliable outputs.

264 Finally, it is worth to remark two major advantages of the ANN2BB procedure with respect to  
265 other hybrid approaches to generate broadband signals based on PBS (see e.g., Mai and Beroza,  
266 2003). First, since the resulting waveform is obtained based on the fit to a regular target response  
267 spectrum, it is possible to avoid the spurious discontinuities of the Fourier spectrum, that are the  
268 typical result of “glueing” around a cross-over frequency the physics-based (LF) signal with the  
269 stochastic one (HF). Second, as thoroughly discussed by Paolucci et al. (2018), in the ANN2BB  
270 procedure the LF and HF portions are not independent, as it is the case for most hybrid approaches,  
271 but their correlation is enforced by the records-trained ANN. This allows the BB-SPEEDset results  
272 to be used to produce realistic earthquake ground motion maps with the proper spatial correlation  
273 also at short periods, as it will be illustrated in the last section of this paper for the case of the

274 L'Aquila earthquake.

275

## 276 **Overview of the BB-SPEEDset: metadata and intensity measures**

277 For each scenario and each selected receiver, a list of source metadata, post-processing metadata,  
278 receiver metadata, site response proxies, source-to-site distances and IMs are computed and stored  
279 in a flat-file (see Table 2 for details). Note that the fields of the flat-file are consistent with the ones  
280 in the Engineering Strong-Motion (ESM) (Lanzano et al., 2018) and the NESS flat-files (Sgobba  
281 et al. 2021). However, when considering a database of PBS results, it is relevant to store  
282 information regarding the type of post-processing accomplished, such as ANN training database,  
283 ANN transition period, broadband procedure, as done in BB-SPEEDset.

284 Since directional effects may be significant in the near-source region, each IM is defined on  
285 different horizontal directions, besides the vertical one, namely: the fault normal (FN) and fault  
286 parallel (FP) components, calculated rotating the horizontal waveforms orthogonal and parallel to  
287 the strike of the fault, respectively; the horizontal geometric mean (HGM), computed using the  
288 two horizontal EW and NS components; the maximum (RotD100) and the median (RotD50) values  
289 of IMs over all orientations (Boore, 2010), denoted in the following by D100 or D50, respectively.

290 In addition to standard peak IMs, such as Peak Ground Acceleration (PGA), Peak Ground Velocity  
291 (PGV), Peak Ground Displacement (PGD) and response spectral accelerations (SA), a variety of  
292 integral and frequency-related IMs is included, such as the Housner Intensity (HI), the Cumulative  
293 Absolute Velocity (CAV), the Arias Intensity (IA), the IA-based durations (i.e., time interval  
294 between 5% and 95% of the total IA, D<sub>s595</sub>, and between 5% and 75%, D<sub>s575</sub>; see Trifunac and  
295 Brady, 1975, Bommer and Martinez-Pereira, 1999) and the mean period (Rathje et al. 1998).  
296 Furthermore, in the flat-file compilation, special care was given to the characterization of pulse-

297 like waveforms, which are of particular interest in earthquake engineering applications owing to  
298 their increased damage potential. Impulsive ground motions reflect two main physical effects.  
299 First, in forward-directivity conditions, the constructive superimposition of waves generated by a  
300 propagating rupture in front of a site may yield double-sided velocity pulses. Second, the  
301 contribution of waves generated by a finite dislocation on the fault plane can produce a permanent  
302 displacement (i.e. fling step) which results in a one-sided velocity pulse. As further discussed in  
303 the following, it is worth underlining that PBS can provide accurate predictions of displacement  
304 waveforms, including static offsets, which are hardly retrieved from recordings, because of the  
305 baseline drifts associated with errors in instrument response at low frequencies. The identification  
306 of pulse-like waveforms and of pulse period ( $T_p$ ) has been done relying on the algorithm proposed  
307 by Shahi and Baker (2014). A thorough discussion on impulsive ground motions will be provided  
308 later in the paper (see Section Analysis of impulsive ground motions).

309 The distribution of BB-SPEEDset data with respect to magnitude and distance is given in Figure  
310 4. The dataset includes a total of 12058 three-component waveforms from earthquake scenarios  
311 with  $M_w$  from 5.5 to 7.4 and Joyner-Boore distances ( $R_{jb}$ ) up to 80 km. Strike-slip, normal and  
312 thrust events are included in the dataset. Most records refer to normal (50%) and strike-slip (41%)  
313 focal mechanisms, while only 9% is from thrust earthquakes (i.e., only the 2012 Po Plain event,  
314 see Table 1). The dominance of normal and strike-slip faults is because, on one hand, normal  
315 events are typical of the seismicity in Central Italy (mostly represented within the BB-SPEEDset)  
316 and, on the other hand, a significant set of strike-slip events from the North Anatolian Fault  
317 (Istanbul case study, see Infantino et al. 2021a) and from the 2016 Kumamoto sequence (Sangaraju  
318 et al. 2021) is also included.

319 In the same figure, the distribution of the NESS dataset is illustrated for comparison. Although the

320 BB-SPEEDset does not cover yet earthquakes with  $M_w \geq 7.5$  (and for this reason the comparisons  
321 shown hereafter will neglect this range), it can be seen that PBS allow to approach an ideally dense  
322 sampling at short distances, that cannot be obtained by the NESS recording stations.

323 The distribution of BB-SPEEDset with respect to site conditions, parametrized in terms of the  
324  $V_{S30}$ , is shown in Figure 5. About 40% of data corresponds to soil conditions with  $V_{S30} < 800$  m/s,  
325 and about 60% to rock conditions, with dominance for hard rock sites with  $V_{S30}$  larger than 1000  
326 m/s. Within the soil classes, the majority of waveforms is on stiff soil with  $V_{S30} > 400$  m/s, but an  
327 appreciable number of data is on very soft sites with  $V_{S30}$  as low as 150 m/s (Marsica case study).  
328 Figure 5 highlights another potential advantage of the simulated datasets: seismo-stratigraphic  
329 conditions are fully known in the PBS, so that each receiver may easily be associated to different  
330 proxies related to site response. Furthermore, site conditions that are typically poorly represented  
331 in the recorded datasets, such as rock and very soft sites, may be better sampled. This may provide  
332 further constraints, complementary to those from earthquake recordings, for the calibration of site  
333 amplification factors, especially in complex geological conditions.

334 As a final remark, note that, BB-SPEEDset should be considered as a dynamically growing dataset,  
335 the scenarios of which may increase in a short time by extending to the case studies listed in Table  
336 1 and not processed yet. Furthermore, new scenarios may specifically be developed to fill in the  
337 magnitude, distance and site conditions gaps of the present version.

338  
339

### **Statistical distributions of ground motion intensity measures**

340 As remarked in the introductory section, a crucial step for the potential use of the BB-SPEEDset  
341 flat-file and signals for engineering applications is to compare the statistical distributions of  
342 different IMs, their attenuation with distance, the features of directional and impulsive near-source



343 accelerograms, with those obtained from recorded ground motions, in order to verify the presence  
344 of potential biases and to identify their sources. For this purpose, since the SPEED results  
345 essentially refer to near-source conditions, we considered as a reference the NESS dataset  
346 introduced previously.

347 Figure 6 shows the cumulative distribution function of different IMs, namely, PGA, PGV,  
348 SA(1.0s), SA(3.0s), CAV, Ds595, IA and HI, as computed from the entire BB-SPEEDset flat-file.  
349 For all IMs, the D50 component is considered. To verify the consistency of our results against  
350 recordings, the statistical distributions derived from BB-SPEEDset are compared in Figure 6 with  
351 those obtained on the NESS dataset, within similar ranges of  $M_w$  and distances as covered by BB-  
352 SPEEDset. As a matter of fact, for this comparison, only records with  $M_w < 7.5$  are considered  
353 (corresponding to about 55% of NESS, see shaded region in Figure 4), consistently with BB-  
354 SPEEDset, but, at low magnitude, larger distances are covered by BB-SPEEDset. To emphasize  
355 the comparison between the two independent sets of data, the lognormal distributions, fitting the  
356 empirical ones, are also superimposed and the corresponding statistical moments are provided.  
357 Furthermore, for each IM distribution, the values of ground motion with a probability of  
358 exceedance less than 5% (i.e. 95<sup>th</sup> percentile of the related distributions) are highlighted on the  
359 graph. Overall, it is remarkable that a full consistency is found between BB-SPEEDset and NESS,  
360 as it should be, as the distribution of  $M_w$  and  $R_{jb}$  of the two datasets are also consistent (apart from  
361 slight differences, as commented above). Although the BB-SPEEDset tends to underestimate the  
362 recorded values of PGA by a factor of about 20%, probably owing to the difficulty of the ANN2BB  
363 approach to describe the short periods as accurately as the long periods, the statistical distributions  
364 of several IMs, from peak measures to integral ones, are noticeably similar both in terms of median  
365 and standard deviation ( $\sigma_{\log 10}$ ). The agreement of PGV, SA(1.0s), CAV and HI is excellent. For

366 SA(3.0s), BB-SPEEDset tends to provide more severe ground motions, most likely because of the  
367 intrinsic higher coherency of waveforms simulated by means of numerical models which  
368 inevitably cannot account for the actual small-scale heterogeneities and complexities in the source,  
369 path and site. Referring to IA, some discrepancies are found especially at intensity values lower  
370 than the median values (median from BB-SPEEDset is lower than NESS of a factor of about 25%),  
371 but the agreement improves significantly above the median. As a matter of fact, the 95<sup>th</sup> percentiles  
372 from BB-SPEEDset and NESS differ of less than 10%. While in most cases the standard deviations  
373 from BB-SPEEDset and NESS are comparable, differences are found for the duration  $D_{s595}$ ,  
374 being  $\sigma_{\log_{10}}$  from BB-SPEEDset lower (0.18) with respect to the one from NESS (0.25), suggesting  
375 that the level of waveform complexity achieved through SPEED simulations is still lower than  
376 reality.

377 As a further consistency check, the distribution of SA(0.1s) and SA(5.0s) obtained from BB-  
378 SPEEDset is compared with that from NESS ( $M_w < 7.5$ ) in Figure 7. It turns out that the correlation  
379 between long and short periods of BB-SPEEDset (the latter ones being a direct output of the  
380 ANN2BB procedure described previously) is consistent with the one from NESS, with few  
381 exceptions of NESS values having a combination of high short-period and low long-period spectral  
382 ordinates, not present in the simulated waveforms.

383

### 384 **Ground motion attenuation with distance**

385 Attenuation of ground motion IMs with distance for the BB-SPEEDset and NESS are compared  
386 in this section. Figure 8 shows PGA and SA(1s) as a function of  $R_{jb}$ , using D50 component, for  
387 different  $M_w$  ranges. No discrimination of soil conditions has been made. The agreement is  
388 reasonably good, with a similar trend of IMs with distance. As already mentioned, there is a

389 tendency of PGAs of the BB-SPEEDset to lie on the lower side of recorded values, especially in  
390 the lower  $M_w$  range. Spectral ordinates at intermediate periods, SA(1s), show a better agreement  
391 with NESS, at any distance. A large but comparable scatter can be observed for the two datasets,  
392 slightly larger for SA(1s). The larger scatter for  $M_w$  around 7.0 and  $R_{jb} > 10\text{km}$  is related to the  
393 Istanbul simulations, that do not have receivers at shorter distances from the source. The high  
394 NESS spectral accelerations at 1s for  $M_w$  in the 6.3-6.7 range and  $R_{jb} > 10\text{km}$  are mostly related to  
395 the 1994 Northridge earthquake, while the lowest values (in the same  $M_w$  and  $R_{jb}$  ranges) are for  
396 the 2014 Aegean Sea earthquake of  $M_w$  6.4. The very low SA(1s) values for  $M_w$  in the 6.8-7.2  
397 range and  $R_{jb} > 20\text{km}$  are related to the Japanese earthquake of 2008.  
398 Figure 9 shows attenuation with  $R_{jb}$  for the Ds595 duration of ground motion. Again, an overall  
399 good agreement among the two datasets is noticeable, with NESS records showing a greater scatter  
400 probably because of their higher complexity than simulated waveforms, as previously noted.  
401 Except for this remark, simulated durations provide a consistent trend with magnitude and  
402 distance.

403

### 404 **Directionality and vertical-to-horizontal motions**

405 It is widely recognized that, in proximity of the source, earthquake ground motion may exhibit  
406 specific features (e.g., Stewart et al., 2001), including polarization related to the fault mechanism  
407 and large, short-period, vertical components exceeding, even significantly, the corresponding  
408 horizontal ones (Bommer et al. 2011, Gülerce and Abrahamson 2011). These aspects will be  
409 addressed in this section, with special care again to the comparison with recordings.

410 Figure 10 shows the median ( $\pm\sigma$ , shaded regions) FN/FP (top) and V/D50 (bottom) for PGA, PGV  
411 and SA(3s), as a function of  $R_{jb}$ , as obtained from BB-SPEEDset and NESS ( $M_w < 7.5$ ). Note that,

412 while long-period components of ground motion are directly related to the PBS results, short-  
413 period components, such as PGA, reflect the output of the ANN2BB procedure. Referring to the  
414 FN/FP distribution, an excellent agreement is found both in terms of median value and variability  
415 at different distances from the source. As expected, both datasets show that in near-source  
416 conditions the FN motion is stronger than the FP at intermediate and long periods and at very short  
417 distance,  $R_{jb} < 5$  km. At increasing distances, the FN polarization tends to vanish, in agreement with  
418 previous studies (Somerville et al. 1997, Pacor et al. 2018). On the other hand, at short periods, no  
419 polarization effects are found, with median FN/FP ratios equal to approximately one at all  
420 distances, both in the BB-SPEEDset and in NESS. Note that, especially at long periods, the  
421 variability across periods is rather large, meaning that directionality features are region- and  
422 scenario-specific. Here, the variability of simulated waveforms tends to be slightly larger but  
423 differences remain limited. Further insights on the physical reasons of such variability could be  
424 obtained by analyzing the dependence on the focal mechanism and the spatial distribution of such  
425 ratios for specific rupture scenarios.

426 As regards the V/D50 ratios, there is a good agreement in terms of PGA (median V/D50  $\sim 0.6$  for  
427 both datasets, but with larger variability for NESS), while for PGV and SA(3s) the BB-SPEEDset  
428 values at very short distance (median V/D50  $\sim 0.6$ ) are higher than NESS (median V/D50  $\sim 0.4$ ).  
429 More detailed studies are planned to investigate the dependence of such different ratios on the  
430 focal mechanism and site conditions.

431

## 432 **Analysis of impulsive ground motions**

433 This section focuses on the identification and comparison of pulse signals, together with the  
434 corresponding period  $T_p$ , tagged and stored in both BB-SPEEDset and NESS flat-files.

435 Figure 11 shows  $T_p$  values, calculated following the algorithm proposed by Shahi and Baker  
436 (2014), as a function of magnitude, for both BB-SPEEDset and NESS.  $T_p$  ranges from 1 to 12 s,  
437 with amplitudes tending to increase with magnitude (Mavroeidis and Papageorgiou, 2003;  
438 Somerville, 2003), but with the largest values probably related to coupling with deep basin  
439 conditions, such as for the earthquakes of Po Plain,  $M_w$  6.0, and Marsica,  $M_w$  6.7, that are poorly  
440 represented by the NESS dataset. With these limitations in mind in terms of comparison of  
441 datasets, the agreement of the  $T_p$  trends from the two datasets is remarkable.

442 Figure 12 shows the trend of  $T_p$  as a function of PGD/PGV, for NESS (left), and BB-SPEEDset  
443 (right). A reasonably good agreement between the two sets is found, within comparable magnitude  
444 ranges (i.e.,  $M_w$  from 6.0 to 7.4). Note that, to improve the accuracy of the PGD estimations from  
445 the NESS dataset,  $T_p$  and peak values from the e-BASCO baseline corrected waveforms have been  
446 considered (see Sgobba et al. 2021 for details).

447 Closed-form analytical relationships between  $T_p$  and PGD/PGV ratios are also shown in Figure 12  
448 , with thick black and grey lines, calculated based on simple functions that may approximate  
449 impulsive ground motion. These relationships are based on the analytical expressions of the  
450 Fourier spectra of the “Ricker wavelet” and of the “double-impulse” functional forms<sup>1</sup>, for which  
451 the peak of the Fourier spectrum at  $f_p=1/T_p$  can be identified and related to PGV and PGD, as  
452 shown in the top-right of Figure 12 . It is interesting to notice that most data from both sets fall  
453 between the two analytical relationships, suggesting that the variability of impulsive ground  
454 motions may roughly be represented by these two functional families.

---

<sup>1</sup> The Ricker wavelet function is defined by  $v(t) = (1 - 2\alpha^2 t^2) e^{-\alpha^2 t^2}$ , with  $\alpha = \pi f_p$ . The double-impulse function is defined by  $v(t) = 2\pi f_p \sqrt{e} t e^{-\alpha^2 t^2}$ , with  $\alpha = \sqrt{2}\pi f_p$ .  $f_p$  represents in both expressions the frequency corresponding to the peak of the Fourier spectrum. Both pulses are scaled to have unit peak amplitude.

455                   **Query by earthquake of the BB-SPEEDset: the L’Aquila example**

456    In this Section we highlight the information that can be obtained from BB-SPEEDset by selecting  
457    a specific earthquake (*query by earthquake*) and extracting the corresponding waveforms and IMs.  
458    As an explanatory case study, the 2009 April 6 L’Aquila earthquake ( $M_w$  6.2) is considered.  
459    First, as a set of illustrative results of the ANN2BB procedure, Figure 13 shows the broadband  
460    three-component (EW, NS and UD) acceleration, velocity and displacement time histories at  
461    selected receivers, superimposed on the corresponding PGA, PGV and PGD maps. Referring to  
462    Smerzini and Villani (2012) and Evangelista et al. (2017) for a thorough comparison of recorded  
463    and simulated waveforms, it is noted herein that simulated time histories have realistic features in  
464    terms of duration, amplitudes and frequency content, with displacement waveforms showing  
465    permanent displacements related to the co-seismic slip on the fault. Furthermore, the spatial  
466    distribution of peak ground motion values at high frequency (PGA) turns out to be well correlated  
467    with the geological features of the basin (see areas of maximum amplitudes within the basin),  
468    supporting the effectiveness of the ANN2BB approach in establishing a correlation between long  
469    and short period ordinates and, thus, reproducing at short periods physics-based features that are  
470    simulated only at long periods. It is also interesting to note that, moving from maps related to short  
471    periods (PGA) to those related to long periods (PGD), the spatial correlation of ground motion  
472    appears to be characterized by increasing correlation length, as expected, at least from a qualitative  
473    point of view. Quantitative evaluations of spatial correlation of spectral accelerations from  
474    broadband numerical simulations can be found in Infantino et al. (2021b) and in Schiappapietra  
475    and Smerzini (2021).

476    To appreciate the richness of information included in BB-SPEEDset flat-file, Figure 14 shows, for  
477    the same case study of L’Aquila, the maps of different IMs, namely, PGV, CAV, IA,  $T_p$ , HI,

478 Ds595. The FN component is shown for all IMs expect for  $T_p$ . In the latter case, the algorithm by  
479 Shahi and Baker (2014) provides as output the  $T_p$  along the orientation along which the pulse is  
480 the strongest.

481 Note that one of the main outcomes of BB-SPEEDset is related to the possibility of drawing maps  
482 and making quantitative evaluations of spatial correlation of a broad spectrum of IMs, for any  
483 orientation of ground motion, with a level of detail which could not be possible using recordings  
484 owing to their limited number. From the maps of Figure 14 the following comments can be made:

- 485 - areas of maximum intensity of PGV, CAV, HI and IA are concentrated on the surface  
486 projection of the fault and inside the alluvial basin, because of the coupling of site response  
487 with rupture propagation effects;
- 488 - lobes of maximum CAV correlate well with the shape of the basin, also at its South-Eastern  
489 edge;
- 490 - there is an overall similarity between the spatial patterns of PGV and HI, which is not  
491 obvious from their definitions: the former is an instantaneous measure of ground shaking,  
492 while the latter, defined as the area of the pseudo-velocity spectrum (5% damping in this  
493 case) between 0.1 and 2.5 s, is proportional to the maximum kinetic energy stored in an  
494 elastic structure;
- 495 - the areas of pulse-like ground motion occurrence are found typically close the top edge of  
496 the fault, mostly related to up-dip directivity effects, highlighting an interesting correlation  
497 between strong pulse-like motions with the areas of peak values for the FN component (see  
498 left panels of Figure 14);
- 499 - correspondingly to areas with impulsive motions, the lowest values of ground motion  
500 duration are found.

501 Although these comments may be considered to be specific for the L'Aquila earthquake case study,  
502 they convey the idea of the comprehensive picture of earthquake ground motion that can be  
503 obtained from PBS and of the potential outcomes that the analysis of the simulated waveforms  
504 may provide in terms of an improved characterization of near-source ground shaking. As a further  
505 example, Figure 15 shows the maps of permanent displacement,  $D_{perm}$ , computed from BB-  
506 SPEEDset for the L'Aquila case study, along the FP (left), FN (center) and UD (right) components.  
507 Note that, while the fling step is naturally reproduced by physics-based simulation of seismic wave  
508 propagation, the estimation of permanent displacement from earthquake recordings requires  
509 complex signal processing procedures (D'Amico et al. 2019), which are typically subject to high  
510 uncertainties. This points out one of the main advantages of numerical simulations, i.e. to provide  
511 an accurate and detailed picture of the long period components of earthquake ground motion, with  
512 relevant implications for the calibration of ground motion models for peak ground displacement  
513 and displacement spectral ordinates (Cauzzi et al. 2015).  
514 Coherently with the normal focal mechanism of the Paganica fault, responsible of the L'Aquila  
515 earthquake, the ground has undergone a static maximum horizontal offset of around 10 cm (both  
516 on the footwall and hanging wall along the FN and FP directions, respectively) and a maximum  
517 subsidence of about 15 cm on the hanging wall. The latter is consistent with the maximum co-  
518 seismic vertical displacement obtained from both synthetic aperture radar (DInSAR) and GPS  
519 observations (D'Agostino et al. 2012).

520

521

## Conclusions

522 In this paper we have presented the BB-SPEEDset, a new dataset of near-source broadband  
523 earthquake ground motions from 3D physics-based numerical simulations obtained by the spectral



524 element computer code SPEED. This is expected to support research on the characterization of  
525 earthquake ground motions in the proximity of the seismic source and in complex geological  
526 conditions, that cannot be extensively documented based on available records.

527 To produce the dataset, an effective workflow has been devised to post-process raw PBS results  
528 in a homogeneous and repeatable format. The core of the workflow is the generation of broadband  
529 ground motions starting from PBS results, reliable only in the low frequency range, according to  
530 the ANN2BB procedure first proposed in Paolucci et al. (2018) and further improved in this work  
531 to make it suitable for massive processing of simulated waveforms.

532 At the present stage, BB-SPEEDset consists of a total number of 12058 three-component  
533 waveforms from worldwide earthquake scenarios, mostly validated against records, with  $M_w$  from  
534 5.5 to 7.4 and  $R_{jb}$  up to 80 km. Besides source, receiver and post-processing metadata, the BB-  
535 SPEEDset flat-file can provide a large portfolio of ground motion intensity measures, from the  
536 standard peak and spectral measures to integral ones (e.g. HI, CAV, duration, IA), up to parameters  
537 related to impulsive ground motions (e.g. pulse period  $T_p$ ) and long period components of ground  
538 motions, such as  $D_{perm}$ .

539 An extensive set of checks has been performed and documented in this paper to verify that the BB-  
540 SPEEDset provides peak values, integral intensity measures, ratios of long-to-short period spectral  
541 ordinates, features of impulsive ground motions and directionality effects, consistent on a  
542 statistical basis with NESS, a dataset of worldwide near-source records (Sgobba et al., 2021). The  
543 positive outcome of such consistency check was not obvious, because the BB-SPEEDset is the last  
544 step of a series of complex studies, starting from the construction of large scale 3D numerical  
545 models, the simulation of realistic fault rupture scenarios, the source-to-site propagation of seismic  
546 waves in complex geological media, and, finally, a smart post-processing of low-frequency signals

547 to get broadband waveforms using ANN. Although reproducing exactly the recorded ground  
548 motions by PBS is not an objective within reach, this paper shows that it is possible to construct  
549 realistic earthquake ground motion scenarios, and that the resulting waveforms are consistent, in  
550 terms of peak values, duration and frequency content, with records obtained in near-source  
551 conditions.

552 Given this major outcome, we envisage that the BB-SPEEDset, either in the present version or in  
553 the following ones enriched by further simulated scenarios, will serve as the basis for several new  
554 achievements for an improved characterization and engineering usage of near-source earthquake  
555 ground motions, such as:

- 556 - to fill in the gaps, in terms of source-to-site conditions, focal mechanisms, variability of fault-  
557 slip distributions and directivity effects, complex geological conditions, that are present in the  
558 worldwide near-source records datasets and that are not expected to be easily covered in short  
559 time by additional records;
- 560 - in the conditions above, provide region- and site- specific input motions for non-linear structural  
561 analyses of engineered structures, that are presently often carried out using unrealistic scaling  
562 factors on recorded ground motions;
- 563 - to provide accurate predictions of long period components of ground motions, including peak  
564 ground displacements and static offsets, that are hardly retrieved from records because of the  
565 uncertainties associated with the post-processing procedures;
- 566 - to construct region-specific scenarios of earthquake ground shaking, suitable to improve  
567 empirical models of spatial correlation (Infantino et al. 2021b) and spatial coherency of ground  
568 motion (Smerzini 2018), taking advantage of the dense spacing of receivers that can be achieved  
569 in the numerical modelling;

570 - to support the development of non-ergodic models for ground shaking scenarios as a key tool  
571 for enhanced seismic hazard and seismic risk evaluations in large urban areas (Stupazzini et al.,  
572 2021).

### 573 **Data and Resources**

574 The NESS2.0 dataset has been downloaded at <http://ness.mi.ingv.it/> (last accessed March 17<sup>th</sup>  
575 2021). The BB-SPEEDset (v1.0) is available at the website [http://speed.mox.polimi.it/BB-](http://speed.mox.polimi.it/BB-SPEEDset)  
576 [SPEEDset](http://speed.mox.polimi.it/BB-SPEEDset) (last accessed May 18<sup>th</sup> 2021), where both the flat-file and corresponding broadband  
577 waveforms can be downloaded.

### 578 **Acknowledgements**

579 This work has been partially supported by Swissnuclear within the research activity “Development  
580 of advanced numerical approaches for earthquake ground motion prediction”, in the framework of  
581 the Sigma2 project, and by the Department of Civil Protection within the ReLUIS project WP18  
582 “Normative contributions related to seismic action”. The authors wish to thank in particular Marco  
583 Stupazzini, Ilario Mazzieri, Maria Infantino and Karim Tarbali, together with the entire SPEED  
584 team, for their support in the development of SPEED kernel, of the related pre- and post-processing  
585 tools and for their contributions to the simulation of some of the earthquake scenarios that this  
586 work has been based on. The fruitful discussions with Philippe Renault in the framework of the  
587 swissnuclear-Sigma2 project are also gratefully acknowledged. Constructive comments by  
588 Francesca Pacor and by another anonymous reviewer helped improving the paper and are  
589 gratefully acknowledged.

590

591

592

## References

- 593 Ancheta, T.D., R.B. Darragh, J.P. Stewart, E. Seyhan, W.J. Silva, B.S.J. Chiou, K.E. Wooddell,  
594 R.W. Graves, A.R. Kottke, D.M. Boore, T. Kishida, and J.L. Donahue (2013). *PEER NGA-*  
595 *West2 Database*, PEER Report No. 2013/03, Pacific Earthquake Engineering Research Center,  
596 University of California, Berkeley, CA, 134 pp.
- 597 Antonietti, P.F., I. Mazzieri, L. Melas, R. Paolucci, A. Quarteroni, C. Smerzini, and M. Stupazzini  
598 (2020). Three-dimensional physics-based earthquake ground motion simulations for seismic  
599 risk assessment in densely populated urban areas, *Mathematics in Engineering* **3**, no. 2, 1-31,  
600 doi: 10.3934/mine.2021012
- 601 Baker, J.W., S. Rezaeian, C.A. Goulet, N. Luco, and G. Teng (2021). A subset of CyberShake  
602 ground-motion time series for response-history analysis. *Earthquake Spectra*, doi:  
603 10.1177/8755293020981970
- 604 Bielak, J., R.W. Graves, K.B. Olsen, R. Taborda, L. Ramirez-Guzman, S.M. Day, G.P. Ely, D.  
605 Roten, T.H. Jordan, P.J. Maechling, J. Urbanic, Y. Cui, G. Juve (2010). The ShakeOut  
606 earthquake scenario: verification of three simulation sets. *Geophysical Journal International*  
607 **180**, no. 1: 375–404
- 608 Bommer, J.J., and A. Martinez-Pereira (1999). The effective duration of earthquake strong motion,  
609 *Journal of Earthquake Engineering* **3**, 127-172.
- 610 Bommer, J.J., S. Akkar, Ö Kale. (2011). A model for vertical-to-horizontal response spectral ratios  
611 for Europe and the Middle East. *Bulletin of the Seismological Society of America* **101**, no. 4:  
612 1783-1806.

613 Boore, D.M. (2010). Orientation-independent, nongeometric-mean measures of seismic intensity  
614 from two horizontal components of motion. *Bull. Seism. Soc. Am.* **100**, 1830–1835.

615 Bracewell, R. N. (1986). *The Fourier Transform and Its Applications*, Second Ed., McGraw-Hill,  
616 New York.

617 Bradley, B.A., D. Pettinga, J.W. Baker, J. Fraser (2017). Guidance on the Utilization of  
618 Earthquake-Induced Ground Motion Simulations in Engineering Practice. *Earthquake Spectra*  
619 33(3): 809-835.

620 Bradley, B.A., K. Tarbali, R.L. Lee, J. Huang, J. Motha, S.E. Bae, V. Polak, M. Zhu, C. Schill, J.  
621 Patterson and D. Lagrava (2020). Cybershake NZ v19.5: New Zealand simulation-based  
622 probabilistic seismic hazard analysis. Proceedings of the 2020 New Zealand Society for  
623 Earthquake Engineering Annual Technical Conference, 22-24 April 2020, Wellington.

624 Cauzzi, C., E. Faccioli, M. Vanini, and A. Bianchini (2015). Updated predictive equations for  
625 broadband (0.01–10 s) horizontal response spectra and peak ground motions, based on a global  
626 dataset of digital acceleration records, *Bull Earthquake Eng* **13**, 1587–1612, doi:  
627 10.1007/s10518-014-9685-y

628 Chaljub, E., P. Moczo, S. Tsuno, P.Y. Bard, J. Kristek, M. Kaser, M. Stupazzini, and M.  
629 Kristekova (2010) Quantitative comparison of four numerical predictions of 3D ground motion  
630 in the Grenoble valley, France. *Bulletin of Seismological Society of America* **100**, no. 4: 1427–  
631 1455

632 D’Agostino, N., D. Cheloni, G. Fornaro, R. Giuliani, and D. Reale (2012). Space-time distribution  
633 of afterslip following the 2009 L’Aquila earthquake, *Journal of Geophys Research* **117**,  
634 IssueB2, doi: 10.1029/2011JB008523

635 D'Amico, M., R. Puglia, E. Russo, C. Maini, F. Pacor, L. Luzi (2017). SYNTHESIS: a web  
636 repository of synthetic waveforms, *Bull Earthquake Eng*, 15:2483-2496.

637 D'Amico, M., C. Felicetta, E. Schiappapietra, F. Pacor, F. Gallovič, R. Paolucci, R. Puglia, G.  
638 Lanzano, S. Sgobba, and L. Luzi (2019). Fling effects from near-source strong-motion records:  
639 Insights from the 2016 M w 6.5 Norcia, Central Italy, Earthquake. *Seismological Research*  
640 *Letters* **90**(2A): 659–671.

641 Evangelista, L., S. Del Gaudio, C. Smerzini, A. D'Onofrio, G. Festa, I. Iervolino, L. Landolfi, R.  
642 Paolucci, A. Santo, and F. Silvestri (2017). Physics-based seismic input for engineering  
643 applications: a case study in the Aterno River valley, Central Italy, *Bulletin of Earthquake*  
644 *Engineering*, **15**, no. 7, 2645–2671.

645 Fayaz, J., S. Rezaeian, F. Zareian (2021). Evaluation of simulated ground motions using  
646 probabilistic seismic demand analysis: CyberShake (ver. 15.12) simulations for Ordinary  
647 Standard Bridges. *Soil Dynamics and Earthquake Engineering* **141**, no. 106533, 1-12.

648 Galasso, C., P. Zhong, F. Zareian, I. Iervolino, and R.W. Graves (2013). Validation of  
649 groundmotion simulations for historical events using MDoF systems, *Earthquake Engineering*  
650 *and Structural Dynamics* **42**, no. 9: 1395–1412.

651 Gatti, F., S. Touhami, F. Lopez-Caballero, R. Paolucci, D. Clouteau, V.A. Fenrnandes, M. Kham,  
652 and F. Voltaire (2018). Broad-band 3-D earthquake simulation at nuclear site by an all-  
653 embracing source-to-structure approach, *Soil Dynamics and Earthquake Engineering*, **115**,  
654 263–280.

655 Graves, R.W., and Pitarka, A. (2010). Broadband ground-motion simulation using a hybrid  
656 approach, *Bull. Seism. Soc. Am.* **100** 2095–2123.

657 Graves, R.W., T.H. Jordan, S. Callaghan, *et al.* (2011). CyberShake: A Physics-Based Seismic  
658 Hazard Model for Southern California, *Pure Appl. Geophys.* **168**, 367–381, doi:  
659 10.1007/s00024-010-0161-6

660 Graves, R.W., and Pitarka, A. (2015). Refinements to the Graves and Pitarka (2010) broadband  
661 ground-motion simulation method, *Seismological Research Letters* **86**, 75–80.

662 Guidotti, R., M. Stupazzini, C. Smerzini, R. Paolucci, and P. Ramieri (2011). Numerical study on  
663 the role of basin geometry and kinematic seismic source in 3D ground motion simulation of  
664 the 22 February 2011 Mw6.2 Christchurch earthquake, *Seism. Res. Lett.* **82**, no. 6, 767-782.

665 Gülerce, Z., N.A. Abrahamson (2011). Site-specific design spectra for vertical ground motion.  
666 *Earthquake Spectra* **27**, no. 4: 1023-1047.

667 Herrero, A., and P. Bernard (1994). A kinematic self-similar rupture process for earthquakes, *Bull.*  
668 *Seism. Soc. Am.* **84**, 1216-1229.

669 Imperatori, W., and F. Gallovič (2017). Validation of 3D velocity models using earthquakes with  
670 shallow slip: case study of the Mw6.0 2014 South Napa, California, event, *Bull. Seism. Soc.*  
671 *Am.* **107**, 1019-1026.

672 Infantino, M., I. Mazzieri, A.G. Özcebe, R. Paolucci and M. Stupazzini (2021a). 3D Physics-Based  
673 Numerical Simulations of Ground Motion in Istanbul from Earthquakes along the Marmara  
674 Segment of the North Anatolian Fault, *Bull. Seism. Soc. Am.* **110**, no. 6, 2559-2576, doi:  
675 10.1785/0120190235.

676 Infantino, M., C. Smerzini, and J. Lin (2021b). Spatial correlation of broadband ground motions  
677 from physics-based numerical simulations. *Earthquake Engineering Structural Dynamics*,  
678 <https://doi.org/10.1002/eqe.3461>.

679 Irikura, K., and H. Miyake (2011). Recipe for predicting strong ground motion from crustal  
680 earthquake scenarios, *Pure Appl. Geophys* **168**, 85–104.

681 Isbilibiroglu, Y., R. Taborda, and J. Bielak (2015). Coupled Soil-Structure Interaction Effects of  
682 Building Clusters During Earthquakes. *Earthquake Spectra* **31**, no. 1: 463–500.

683 Komatitsch, D., S. Tsuboi, and J. Tromp, (2013). The spectral-element method in seismology.  
684 *Seismic Earth: Array Analysis of Broadband Seismograms*, **157**, 205–227.

685 Lanzano, G., S. Sgobba, L. Luzi, R. Puglia, F. Pacor, C. Felicetta, M. D’Amico, F. Cotton, and D.  
686 Bindi (2018). The pan-European engineering strong motion (ESM) flat-file: Compilation  
687 criteria and data statistics, *Bull. Earthq. Eng.*, **17**, 561–582, doi: 10.1007/s10518-018-0480-z.

688 Leonard M. (2010). Earthquake Fault Scaling: Self-Consistent Relating of Rupture Length, Width,  
689 Average Displacement, and Moment Release, *Bull. Seism. Soc. Am.* **100**, no. 5A, 1971–1988,  
690 doi: 10.1785/0120090189.

691 Lu, X., Y. Tian, G. Wang, D. Huang (2018). A numerical coupling scheme for nonlinear time  
692 history analysis of buildings on a regional scale considering site-city interaction effects,  
693 *Earthquake Engineering and Structural Dynamics* **47**, no. 13: 2708-2725

694 Maeda, T., A. Iwaki, N. Morikawa, S. Aoi, and H. Fujiwara (2016). Seismic-Hazard Analysis of  
695 Long-Period Ground Motion of Megathrust Earthquakes in the Nankai Trough Based on 3D  
696 Finite-Difference Simulation, *Seismological Research Letters* **87**, no. 6, 1265–1273, doi:  
697 10.1785/0220160093.

698 Mai, P.M. and G.C. Beroza (2000). Source scaling properties from finite-fault-rupture models,  
699 *Bull Seism. Soc. Am.* **90**, no. 3, 604–615.



700 Mai, P. M., and G. C. Beroza (2003). A hybrid method for calculating near-source, broadband  
701 seismograms: Application to strong motion prediction, *Phys. Earth Planet. In.* **137**, 1/4, 183–  
702 199.

703 Maufroy, E., E.Chaljub, F: Hollender, J. Kristek, P. Moczo, P. Klin, E. Priolo, A. Iwaki, T. Iwata,  
704 V: Etienne, F. De Martin, N.P. Theodoulidis, M. Manakou, C. Guyonnet-Benaize, K. Pitilakis,  
705 and P.Y. Bard (2015). Earthquake Ground Motion in the Mygdonian Basin, Greece: The E2VP  
706 Verification and Validation of 3D Numerical Simulation up to 4 Hz. *Bulletin of the*  
707 *Seismological Society of America* **105**, no. 3: 1398–1418

708 Mavroeidis, G. P., and A. S. Papageorgiou (2003). A mathematical representation of near-fault  
709 ground motions, *Bull Seism. Soc. Am.* **93**, no. 3, 1099–1131.

710 Mazzieri, I, M. Stupazzini, R. Guidotti, and C. Smerzini (2013) SPEED: SPectral Elements in  
711 Elastodynamics with Discontinuous Galerkin: a non-conforming approach for 3D multi-scale  
712 problems, *Int J Numer Meth Eng* **95**, no. 12, 991–1010.

713 McCallen, D.M., A. Petersson, A. Rodgers, A. Pitarka, M. Miah, F.M. Petrone, B. Sjogreen, N.  
714 Abrahamson, H. Tang (2020a). EQSIM—A multidisciplinary framework for fault-to-structure  
715 earthquake simulations on exascale computers part I: Computational models and workflow.  
716 *Earthquake Spectra*, doi: 10.1177/8755293020970982.

717 McCallen, D.M., F.M. Petrone, M. Miah, A. Pitarka, A. Rodgers, and N. Abrahamson (2020b).  
718 EQSIM—A multidisciplinary framework for fault-to-structure earthquake simulations on  
719 exascale computers, part II: Regional simulations of building response, part II: Regional  
720 simulations of building response. *Earthquake Spectra*, doi:10.1177/8755293020970980.

721 Norme Tecniche per le Costruzioni (2018), *Gazzetta Ufficiale della Repubblica Italiana* **42**, 20  
722 febbraio 2018 (in italian).

723 Özcebe, A. G., C. Smerzini, R. Paolucci, H. Pourshayegan, R. Rodríguez Plata, C.G. Lai, E.  
724 Zuccolo, F. Bozzoni, and M. Villani (2019). On the comparison of 3D, 2D, and 1D numerical  
725 approaches to predict seismic site amplification: the case of Norcia basin during the M6.5 2016  
726 October 30 earthquake, *Proceedings of the 7th International Conference on Earthquake  
727 Geotechnical Engineering*, Rome, 17-20 June 2019.

728 Pacor, F., C. Felicetta, G. Lanzano, S. Sgobba, R. Puglia, M. D'Amico, E. Russo, G. Baltzopoulos,  
729 I. Iervolino (2018). NESS1: A Worldwide Collection of Strong-Motion Data to Investigate  
730 Near-Source Effects, *Seism. Res. Lett.* **89**, no. 6: 2299-2313.

731 Paolucci, R., I. Mazzieri, C. Smerzini, and M. Stupazzini (2014). Physics-based earthquake ground  
732 shaking scenarios in large urban areas. *Perspectives on European Earthquake Engineering and  
733 Seismology, Geotechnical, Geological and Earthquake Engineering*, A. Ansal, **34**.

734 Paolucci, R., I. Mazzieri, and C. Smerzini (2015). Anatomy of strong ground motion: near-source  
735 records and 3D physics-based numerical simulations of the  $M_w$  6.0 May 29 2012 Po Plain  
736 earthquake, Italy, *Geophys. J. Int.* **203**, 2001–2020.

737 Paolucci, R., L. Evangelista, I. Mazzieri, and E. Schiappapietra (2016) The 3D numerical  
738 simulation of near-source ground motion during the Marsica earthquake, central Italy, 100  
739 years later, *Soil Dynamics and Earthquake Engineering* **91**, 39-52.

740 Paolucci, R., F. Gatti, M. Infantino, C. Smerzini, A. G. Özcebe, and M. Stupazzini (2018).  
741 Broadband Ground Motions from 3D Physics-Based Numerical Simulations Using Artificial  
742 Neural Networks, *Bull. Seism. Soc. Am.* **108**, 1272-1286.

743 Paolucci, R., I. Mazzieri, G. Piunno, C. Smerzini, M. Vanini, A.G. Özcebe (2021). Earthquake  
744 ground motion modelling of induced seismicity in the Groningen gas field, *Earthquake  
745 Engineering and Structural Dynamics* **50**, 135–154, doi: 10.1002/eqe.3367.

746 Pilz, M., S. Parolai, M. Stupazzini, R. Paolucci, and J. Zschau (2011). Modelling basin effects on  
747 earthquake ground motion in the Santiago de Chile basin by a spectral element code. *Geophys.*  
748 *J. Int.* **187**, 929–945. doi: 10.1111/j.1365-246X.2011.05183.x.

749 Pitarka, A., R.W. Graves, K. Irikura, *et al.* (2020). Kinematic Rupture Modeling of Ground Motion  
750 from the M7 Kumamoto, Japan Earthquake, *Pure Appl. Geophys.* **177**, 2199-2221, doi:  
751 10.1007/s00024-019-02220-5.

752 Pousse, G., L. Bonilla, F. Cotton, and L. Margerin (2006). Nonstationary stochastic simulation of  
753 strong ground motion time histories including natural variability: Application to the Knet  
754 Japanese database, *Bull. Seism. Soc. Am.*, **96**, no. 6, 2103-2117.

755 Rathje, EM, N.A. Abrahamson, and J.D. Bray (1998). Simplified frequency content estimates of  
756 earthquake ground motions, *J Geotech Geoenviron Eng* **124**, no. 2, 150–159.

757 Sabetta, F., and A. Pugliese (1996). Estimation of response spectra and simulation of nonstationary  
758 earthquake ground motions, *Bull. Seism. Soc. Am.* **86**, no. 2, 337-352.

759 Sabetta, F., Pugliese, A., Fiorentino, G., Lanzano, G. and L. Luzi (2021). Simulation of non-  
760 stationary stochastic ground motions based on recent Italian earthquakes. *Bull Earthquake Eng*,  
761 <https://doi.org/10.1007/s10518-021-01077-1>

762 Sangaraju, S., R. Paolucci, and C. Smerzini (2021) 3D physics-based ground motion simulation of  
763 the 2016 Kumamoto earthquakes, *Proc. 6<sup>th</sup> IASPEI / IAEE International Symposium: The*  
764 *Effects Of Surface Geology On Seismic Motion (ESG6)*, August 2021, Kyoto, Japan.

765 Schiappapietra, E. and C. Smerzini (2021). Spatial correlation of earthquake ground motion in  
766 Norcia (Central Italy) from broadband physics-based simulations, *Bulletin of Earthquake*  
767 *Engineering*, submitted.

768 Schmedes, J., R.J. Archuleta, and D. Lavallée (2012). A kinematic rupture model generator  
769 incorporating spatial interdependency of earthquake source parameters, *Geophysical Journal*  
770 *International* **192**, 1116-1131.

771 Sgobba, S., C. Felicetta, G. Lanzano, F. Ramadan, M. D’Amico, and F. Pacor, (2021). NESS2.0:  
772 an updated version of the worldwide dataset for calibrating and adjusting ground motion  
773 models in near-source, *Bull. Seism. Soc. Am.*, submitted.

774 Shahi, S.K., and J.W. Baker (2014). An Efficient Algorithm to Identify Strong-Velocity Pulses in  
775 Multicomponent Ground Motions, *Bull. Seism. Soc. Am.* **104**, no. 5, 2456–2466. doi:  
776 10.1785/0120130191.

777 Smerzini, C. (2010). *The earthquake source in numerical modeling of seismic wave propagation*  
778 *in heterogeneous Earth media*, PhD Thesis, University School for Advanced Studies in Pavia.

779 Smerzini, C., R. Paolucci, and M. Stupazzini (2011). Comparison of 3D, 2D and 1D numerical  
780 approaches to predict long period earthquake ground motion in the Gubbio plain, Central Italy,  
781 *Bulletin of Earthquake Engineering*, **9**, no. 6, 2007–2029.

782 Smerzini, C., C. Galasso, I. Iervolino, and R. Paolucci (2014). Ground motion record selection  
783 based on broadband spectral compatibility, *Earthq. Spectra* **30**, no. 4, 1427–1448.

784 Smerzini, C., K. Pitilakis, and Hashemi K. (2017). Evaluation of earthquake ground motion and  
785 site effects in the Thessaloniki urban area by 3D finite-fault numerical simulations, *Bulletin of*  
786 *Earthquake Engineering* **15**, no. 3, 787–812.

787 Smerzini, C., and K. Pitilakis (2018). Seismic risk assessment at urban scale from 3D physics-  
788 based numerical modeling: the case of Thessaloniki. *Bulletin of Earthquake Engineering* **16**,  
789 no. 7: 2609-2631.

790 Smerzini, C. (2018). Spatial variability of earthquake ground motion from 3D physics-based  
791 numerical simulations, *Proceedings of the 16th European Conference on Earthquake*  
792 *Engineering*, Thessaloniki, 18-21 June 2018.

793 Smerzini, C., F. Cavalieri, S. Argyroudis, and K. Pitilakis (2018). 3D physics-based numerical  
794 modeling as a tool for seismic risk assessment of urban infrastructural systems: the case of  
795 Thessaloniki, Greece. *Proceedings of the 16th European Conference on Earthquake*  
796 *Engineering*, Thessaloniki, 18-21 June 2018

797 Somerville, P.G., N.F. Smith, R.W. Graves, and N.A. Abrahamson (1997). Modification of  
798 Empirical Strong Ground Motion Attenuation Relations to Include the Amplitude and Duration  
799 Effects of Rupture Directivity. *Seismological Research Letters* **68**, no. 1, 199-222, doi:  
800 10.1785/gssrl.68.1.199.

801 Somerville, P. G. (2003). Magnitude scaling of the near fault rupture directivity pulse, *Physics of*  
802 *the Earth and Planetary Interiors* **137**, 201–212.

803 Stupazzini, M., R. Paolucci, and H. Igel (2009). Near-fault earthquake ground-motion simulation  
804 in Grenoble Valley by high-performance spectral element code, *Bull. Seism. Soc. Am.* **99**, no.  
805 1, 286–301, doi: 10.1785/0120080274.

806 Stupazzini, M., M. Infantino, A. Allmann, and R. Paolucci (2021). Physics-based probabilistic  
807 seismic hazard and loss assessment in large urban areas: A simplified application to Istanbul.  
808 *Earthquake Engng Struct Dyn.* **50**, 99– 115, doi: 10.1002/eqe.3365.

809 Stewart, J.P., S.J. Chiou, J.D. Bray, R.W. Graves, P.G. Somerville, and N.A. Abrahamson (2001).  
810 *Ground Motion Evaluation Procedures for Performance-Based Design*. PEER Report  
811 2001/09.

812 Taborda, R., and J. Bielak (2013). Ground-Motion Simulation and Validation of the 2008 Chino  
813 Hills, California, Earthquake. *Bulletin of Seismological Society of America* **103**, no. 1: 131-  
814 156

815 Taborda, R., and J. Bielak (2014). Ground-Motion Simulation and Validation of the 2008 Chino  
816 Hills, California, Earthquake Using Different Velocity Models, *Bulletin of Seismological*  
817 *Society of America* **104**, no. 4: 1876-1898

818 Trifunac, M.D., and Brady, A. G. (1975). A study on the duration of strong earthquake ground  
819 motion, *Bull. Seism. Soc. Am.* **65**, no. 3, 581-626.

820 Thingbaijam K.K.S., and P.M. Mai (2016). Evidence for truncated exponential probability  
821 distribution of earthquake slip, *Bull. Seism. Soc. Am.* **106**, no. 4, 1802–1816.

822 Villani M., E. Faccioli, M. Ordaz, and M. Stupazzini (2014). High-resolution seismic hazard  
823 analysis in a complex geological configuration: the case of the Sulmona basin in Central Italy,  
824 *Earthq. Spectra* **30**, no. 4, 1801–1824.

825 Wells, D., and K. Coppersmith, (1994). New Empirical Relationships among Magnitude, Rupture  
826 Length, Rupture Width, Rupture Area, and Surface Displacement, *Bull. Seism. Soc. Am.* **84**,  
827 974-1002.

828

829

**Full mailing address for each author**

830 Roberto Paolucci

831 Department of Civil and Environmental Engineering, Politecnico di Milano

832 Piazza Leonardo da Vinci, 32 – 20133 Milano, Italy.

833 E-mail: [roberto.paolucci@polimi.it](mailto:roberto.paolucci@polimi.it).

834

835 Chiara Smerzini

836 Department of Civil and Environmental Engineering, Politecnico di Milano

837 Piazza Leonardo da Vinci, 32 – 20133 Milano, Italy.

838 E-mail: [chiara.smerzini@polimi.it](mailto:chiara.smerzini@polimi.it)

839

840

841 Manuela Vanini

842 Department of Civil and Environmental Engineering, Politecnico di Milano

843 Piazza Leonardo da Vinci, 32 – 20133 Milano, Italy.

844 E-mail: [manuela.vanini@polimi.it](mailto:manuela.vanini@polimi.it).

845

846

847

849 **Table 1** Numerical simulations performed by the code SPEED.  $M_w$  = moment magnitude, SoF =  
850 Style of Faulting (SS=Strike-Slip, NF=Normal Fault, TF=Thrust Fault),  $V_{s,min}$ =minimum shear  
851 wave velocity,  $f_{max}$ =maximum frequency of the numerical model. The scenarios included in BB-  
852 SPEEDset are specified in the last column.

Case Study	Fault (SoF)	$M_w$	Model size (km <sup>3</sup> )	$V_{s,min}$ (m/s)	$f_{max}$ (Hz)	Event for validation	References	Included in BB-SPEEDset
Grenoble, France	Belledonne (SS)	6.0	41x50x8	300	3	Benchmark	Stupazzini et al. (2009)	not included yet
Gubbio plain, Central Italy	Colfiorito (NF)	6.0	85x62x10	250	3	26 Sept 1997	Smerzini et al. (2011)	not included yet
Tagliamento plain, Northern Italy	Gemona Faults (TF)	6.1	57x53x12	300	2.5	15 Sept 1976	Smerzini (2010)	not included yet
L'Aquila, Central Italy	Paganica (NF)	6.2	58x58x20	300	2.0	6 Apr 2009	Evangelista et al. (2017)	6.2 Aquila 2009
Sulmona, Central Italy	Mt. Morrone (NF)	6.0	49x42x13	500	2.5	Ideal scenarios	Villani et al. (2014)	6.0 SulmonaS03
		6.5						6.0 SulmonaS04
								6.5 SulmonaS03
								6.5 SulmonaS05
Christchurch, New Zealand	Lyttelton (TF)	6.3	60x60x20	300	2.0	22 Feb 2011	Guidotti et al. (2011)	not included yet
Po Plain, Northern Italy	Mirandola (TF)	6.0	74x51x20	300	1.5	29 May 2012	Paolucci et al. (2015)	6.0 Emilia 2012
Marsica, Central Italy	Fucino (NF)	6.7	56x46x20	100	2.0	13 Jan 1915	Paolucci et al. (2016)	6.7 Marsica 1915
Thessaloniki, Northern Greece	Gerakarou (NF)	6.5	82x64x31	300	1.5	20 Jun 1978	Smerzini et al. (2017)	6.5 Salonicco 1978
	Anthemountas (NF)	7.0				Ideal scenario	Smerzini et al. (2018)	7.0 SaloniccoS01
Norcia, Central Italy	Mt. Vettore-Mt. Bove (NF)	6.5	50x40x21	280	1.5	30 Oct 2016	Özcebe et al. (2019)	6.5 Norcia 2016
		5.8						5.8 NorciaS01



Case Study	Fault (SoF)	M <sub>w</sub>	Model size (km <sup>3</sup> )	V <sub>s,min</sub> (m/s)	f <sub>max</sub> (Hz)	Event for validation	References	Included in BB-SPEEDset
		5.5				Ideal scenarios		5.5 NorciaS01
Wellington, New Zealand	Wellington–Hutt (SS)	6.0-7.0	80x50x45	300	2.0	Ideal scenarios	Paolucci et al. (2014)	not included yet
Santiago, Chile	San Ramon (TF)	6.0 6.5 7.0	97x77x19	400	2.0	1 Apr 2010	Pilz et al. (2011)	not included yet
Istanbul, Turkey	North Anatolian Fault - Marmara Sea (SS)	5.7	165x100x30	250	1.5	26 Sept 2019	Infantino et al. (2021a)  Stupazzini et al. (2021)	not included yet
		7.0				Ideal scenarios		7.0 IstanbulS16 7.0 IstanbulS20 7.0 IstanbulS23
		7.2				Ideal scenarios		7.2 IstanbulS05 7.2 IstanbulS09 7.2 IstanbulS19
		7.4				Ideal scenarios		7.4 IstanbulS02 7.4 IstanbulS12 7.4 IstanbulS20
Beijing, China	Shunyi-Qianmen-Liangxiang (TF)	6.5 6.9 7.3	70x70x30	200	1.5	Ideal scenarios	Antonietti et al. (2020)	not included yet
Groningen, the Netherlands	NF	3.4	20x20x5	150	10	8 Jan 2018	Paolucci et al. (2021)	not included yet
Kumamoto, Japan	Hinagu-Futagawa-Aso Caldera (SS)	7.0	53*46*22	500	1.5	15 Apr 2016 (16:25 UTC)	Sangaraju et al. (2021)	7.0 Kumamoto2016
	Hinagu-Futagawa (SS)	6.1				14 Apr 2016 (12:26 UTC)		not included yet
	Aso Caldera (SS)	5.5				15 Apr 2016 (18:03 UTC)		not included yet

853

854

855

856 **Table 2** Structure of the BB-SPEEDset flat-file.

<b>Source Metadata</b>	Scenario ID	Hypocenter Lat/Lon/Depth	Strike, Dip, Rake	Fault mechanism
	Event ID	$M_w$	References	Rupture top
	Scenario ID card	$M_o$	ANN database	Fault Vertices (*)
	Event_Time	Average slip	Transition period	Length (*)
	Event Nation Code	No. segments	ANN2BB procedure	Width (*)
<b>Receiver Metadata</b>	Receiver ID			
	Receiver East/North coordinates			
	Receiver elevation			
<b>Site Response Proxies</b>	$V_{S30}$	$H_{bed}$ (depth of the alluvial-bedrock interface)	$V_{Sbed}$ (time averaged $V_s$ from the surface to $H_{bed}$ )	
	$V_{Seq}$	$H_{800}$ (depth to $V_s \geq 800$ m/s)	$V_{S800}$ (time averaged $V_s$ from the surface to $H_{800}$ )	
<b>Source-to-Site Distances</b> (†)	Epicentral dist.	R_line	Joyner and Boore distance, $R_{jb}$	
	Hypocentral dist.	$R_x$	$R_{rup}$	
<b>Intensity Measures</b> (‡)	PGA	SA(T) for T from 0.01 to 10 s	Pulse-like flag	Housner Intensity
	PGV	Permanent displacement	Pulse period	Arias Intensity
	PGD	Mean period	$D_{s595}$ , $D_{s575}$	Cumulative Absolute Velocity

857 (\*) Fault dimensions are given with respect to 'numerical fault' and 'effective fault'

858 (†) Distances from the fault are computed with respect to its "effective" dimensions

859 (‡) Except pulse features, Intensity Measures are defined for the following directions: NS, EW =  
860 horizontal; UD = vertical; HGM= horizontal geometrical mean; FN=Fault Normal; FP=Fault Parallel; D50  
861 = median value of the IM distribution obtained from rotated waveforms; D100 = maximum value of the IM  
862 distribution obtained from rotated waveforms. (Rotation angles are given as well.)

863

864

865

866

867

868

869

870

## List of Figure Captions

871 **Figure 1** Workflow for post-processing of SPEED results and creation of the corresponding flat-  
872 file for BB-SPEEDset.

873 **Figure 2** Computation of the effective fault dimensions according to the procedure proposed by  
874 Mai and Beroza (2000) and extended by Thingbaijam and Mai (2016).

875 **Figure 3** Flowchart of the ANN2BB approach revised after Paolucci et al. (2018) for the massive  
876 processing of PBS for broadband computation and compilation of BB-SPEEDset.

877 **Figure 13**  $M_w$  6.2 L'Aquila 2009: peak ground motion maps (left: PGA; center: PGV; right: PGD)  
878 and selected broadband waveforms (left: acceleration; center: velocity; right: displacement), EW  
879 component, from BB-SPEEDset.

880 **Figure 14**  $M_w$  6.2 L'Aquila 2009: maps of different ground motion IMs stored in BB-SPEEDset,  
881 a) PGV; b) Cumulative Absolute Velocity (CAV); c) Arias Intensity (IA); d) pulse period ( $T_p$ ); e)  
882 Housner Intensity (HI); f) Duration between 5% and 95% of total IA (Ds595). For all IMs, except  
883  $T_p$ , the FN component is shown.

884 **Figure 15**  $M_w$  6.2 L'Aquila 2009: maps of permanent displacement ( $D_{perm}$ ) on the three  
885 components of motion, a) FP; b) FN; c) UD.

886 **Figure 4**  $M_w$  and  $R_{jb}$  distribution of BB-SPEEDset (gray circles), in comparison with that from  
887 NESS dataset (black dots, after Sgobba et al. 2021). The shaded region indicates the records  
888 excluded from the comparisons reported in this work.

889 **Figure 5** Distribution of BB-SPEEDset with respect to  $V_{s30}$ .

890 **Figure 6** Cumulative distribution functions of PGA, PGV, SA(1.0s), SA(3.0s), CAV, Ds595, IA  
891 and HI, as obtained from BB-SPEEDset (dark gray: empirical; black: best-fitting lognormal

892 distribution with corresponding statistical moments) and from NESS (light gray and dashed lines).  
893 The 95<sup>th</sup> percentiles of the statistical distributions are also superimposed on the graph. For all IMs,  
894 the D50 component is considered.

895 **Figure 7** SA(0.1s) and SA(5s) distribution from BB-SPEEDset (dark gray) in comparison with  
896 that from NESS (light gray) in the same range of magnitude. The D50 component is considered  
897 for both spectral accelerations.

898 **Figure 8** D50 components of PGA (top) and SA(1s) (bottom) as a function of  $R_{jb}$  distance, for  
899 BB-SPEEDset (dark gray) and NESS (light gray), considering different  $M_w$  ranges (centered  
900 around 6.0, 6.5 and 7.0).

901 **Figure 9** Duration  $D_{s595}$  (for D50 component) versus  $R_{jb}$  distance, for both BB-SPEEDset (dark  
902 gray) and NESS (light gray), for different  $M_w$  ranges (centered around 6.0, 6.5 and 7.0).

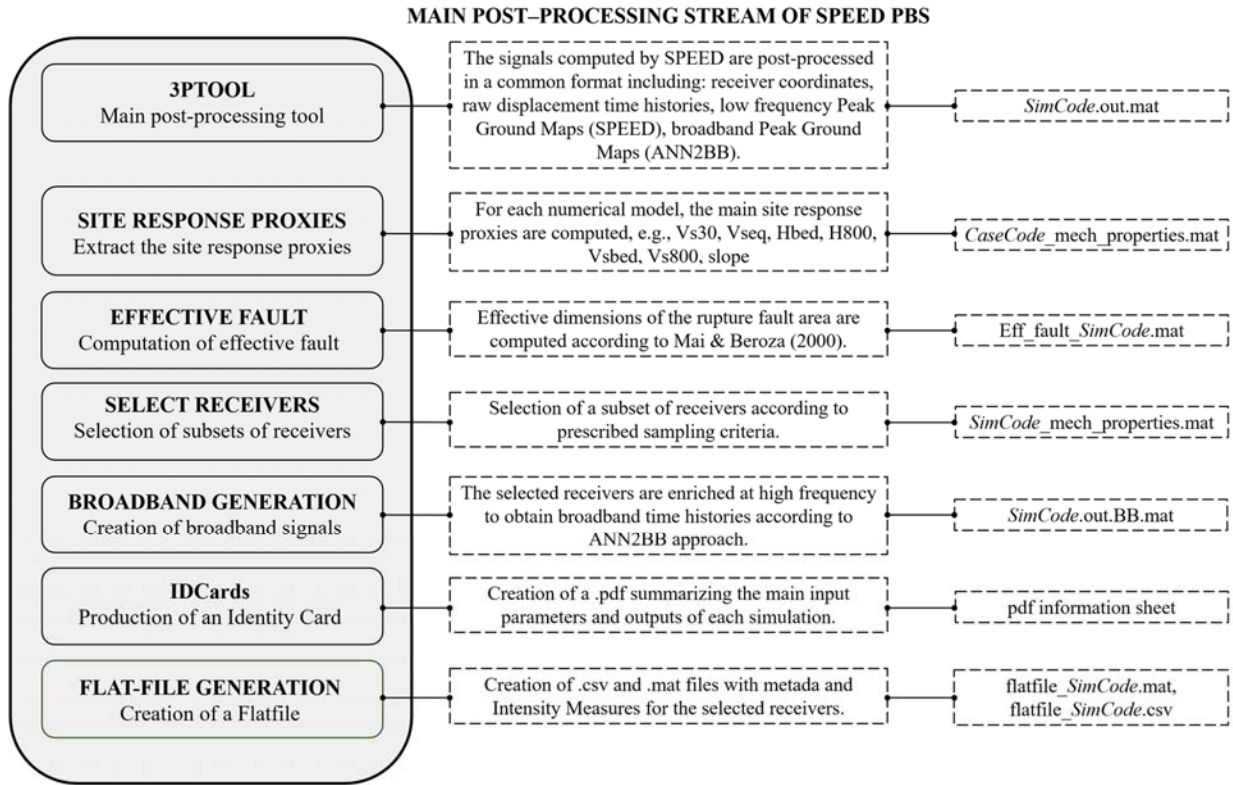
903 **Figure 10** Ratios of FN/FP (top) and of V/D50 (bottom) for PGA (left), PGV (center) and SA(3s)  
904 (right), as a function of  $R_{jb}$ . The median  $\pm\sigma$  ratios from BB-SPEEDset (dark grey) and NESS (light  
905 grey) are compared.

906 **Figure 11** Pulse period  $T_p$  versus earthquake magnitude for observed pulse-like ground motions  
907 of BB-SPEEDset (20% of set data, in light gray) and NESS dataset (almost 30% of whole set data,  
908 in black).

909 **Figure 12** Pulse period  $T_p$  as a function of PGD/PGV for the BB-SPEEDset dataset (right) and for  
910 the NESS dataset (left), for different magnitude ranges, together with analytical relationships for  
911 Ricker wavelet and double-impulse functions.

912

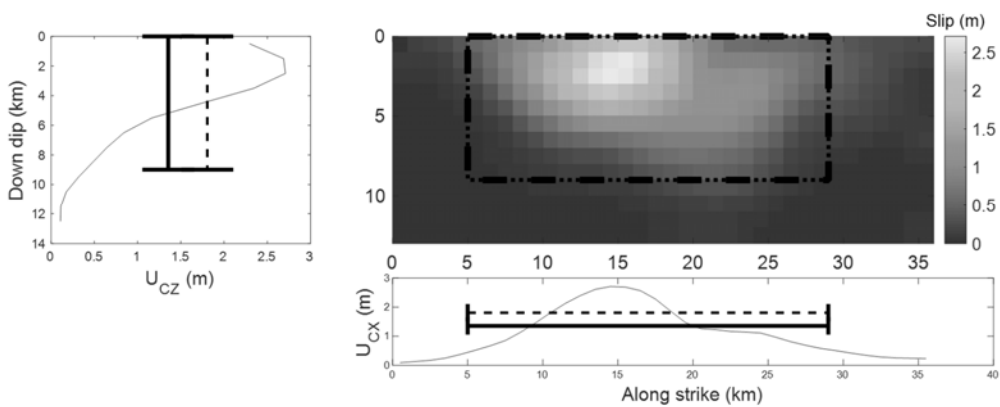
Figures



914

915 **Figure 1** Workflow for post-processing of SPEED results and creation of the corresponding flat-

916 file for BB-SPEEDset.

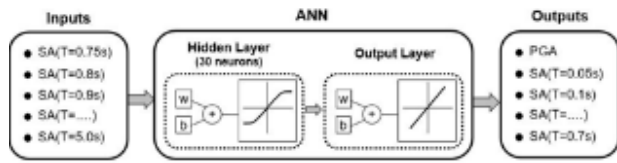


917

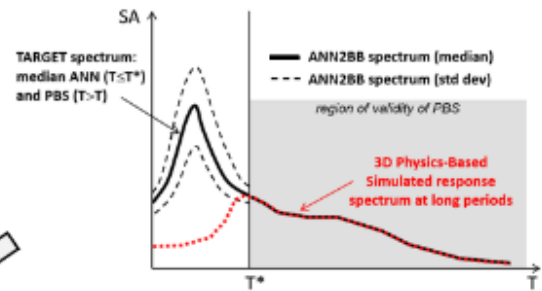
918 **Figure 2** Computation of the effective fault dimensions according to the procedure proposed by

919 Mai and Beroza (2000) and extended by Thingbaijam and Mai (2016).

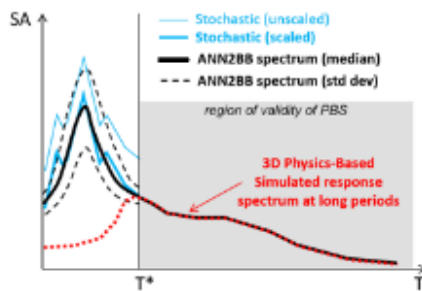
(1) Training of an Artificial Neural Network (ANN) based on a dataset of strong-motion recordings



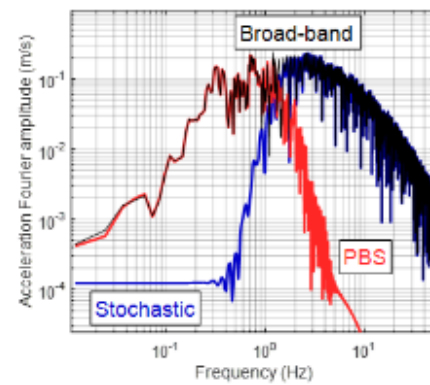
(2) Application of ANN to predict short period spectral ordinates based on PBS results ( $T \geq T^*$ )



(3) Simulation and linear scaling of a stochastic signal to approach the target ANN2BB spectrum



(4) Combination of stochastic and PBS signals



920

921 **Figure 3** Flowchart of the ANN2BB approach revised after Paolucci et al. (2018) for the massive  
 922 processing of PBS for broadband computation and compilation of BB-SPEEDset.

923

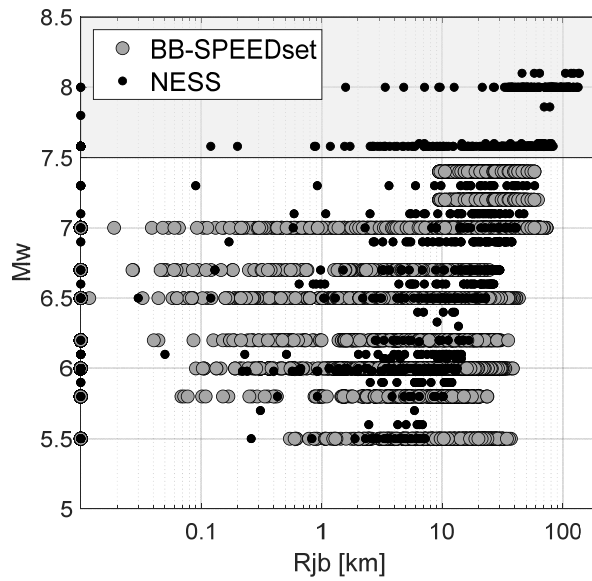
924

925

926

927

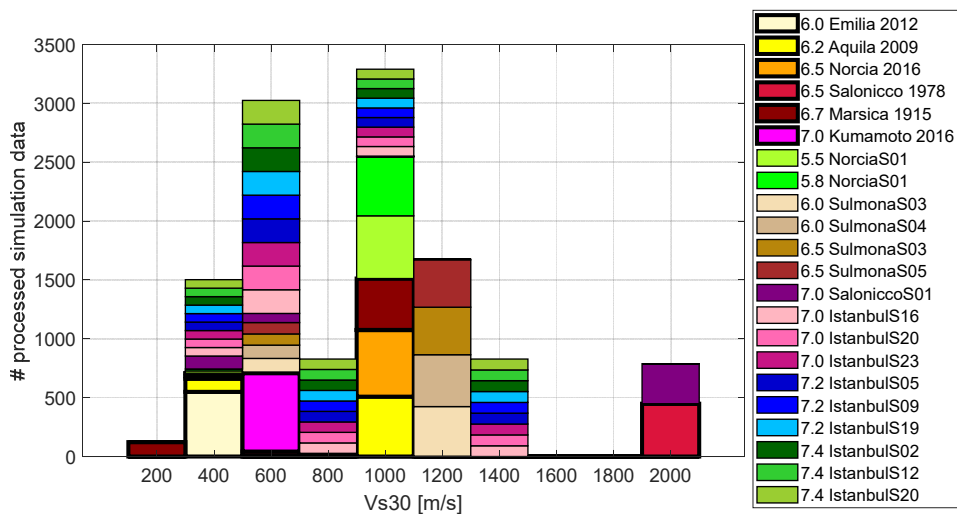
928



929

930 **Figure 4**  $M_w$  and  $R_{jb}$  distribution of BB-SPEEDset (gray circles), in comparison with that from  
 931 NESS dataset (black dots, after Sgobba et al. 2021). The shaded region indicates the records  
 932 excluded from the comparisons reported in this work.

933

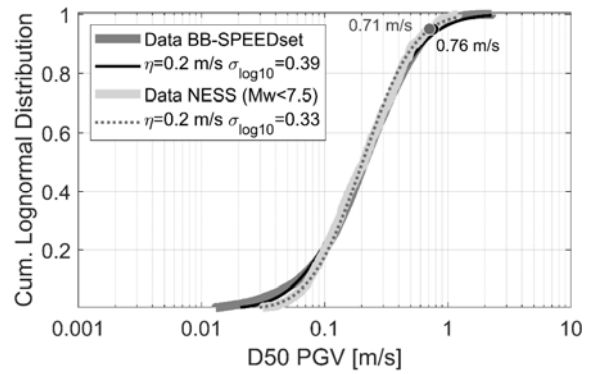
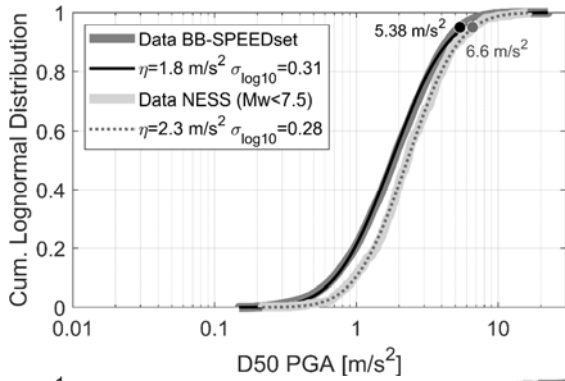


934

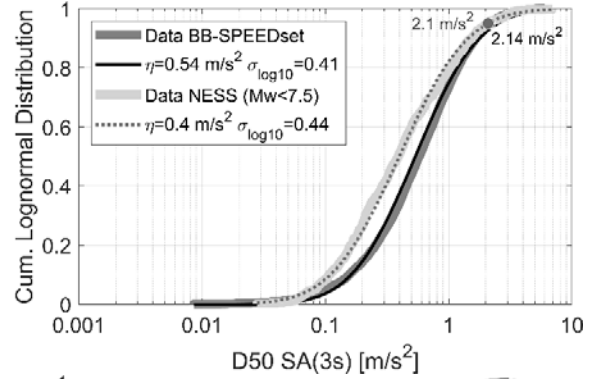
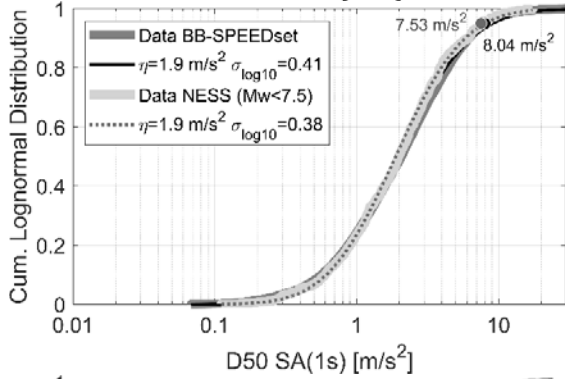
935 **Figure 5** Distribution of BB-SPEEDset with respect to  $V_{s30}$ .

936

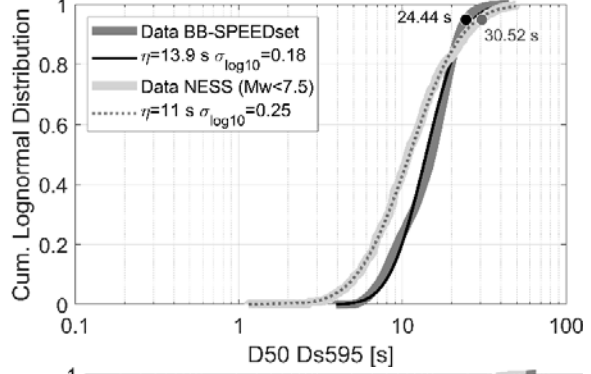
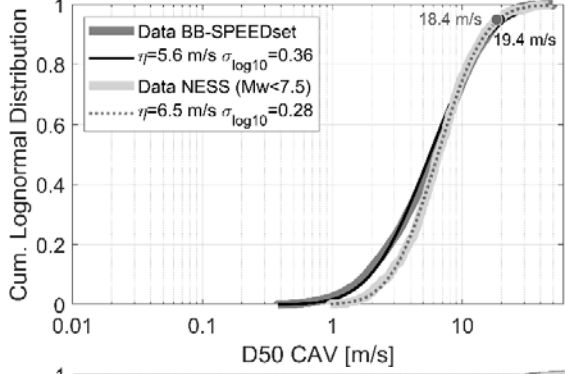
937



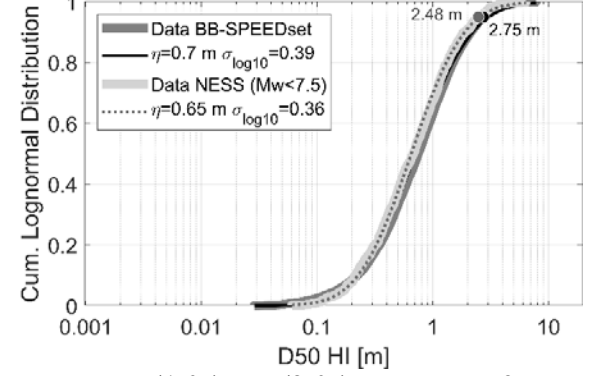
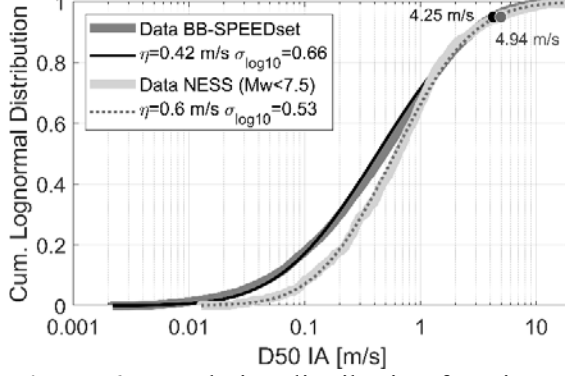
938



939



940



941 **Figure 6** Cumulative distribution functions of PGA, PGV, SA(1.0s), SA(3.0s), CAV, Ds595, IA

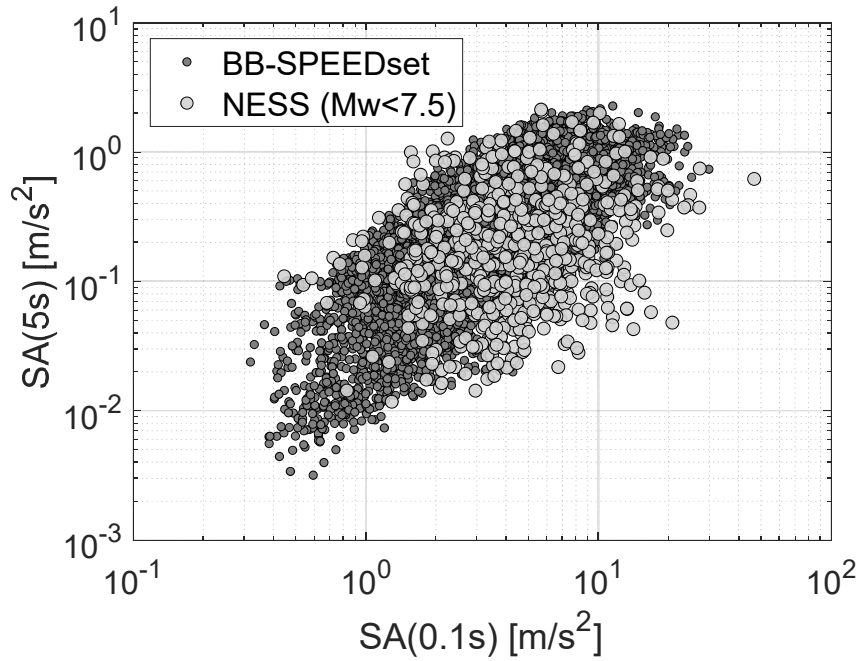
942 and HI, as obtained from BB-SPEEDset (dark gray: empirical; black: best-fitting lognormal

943 distribution with corresponding statistical moments) and from NESS (light gray and dashed lines).



944 The 95<sup>th</sup> percentiles of the statistical distributions are also superimposed on the graph. For all IMs,  
945 the D50 component is considered.

946



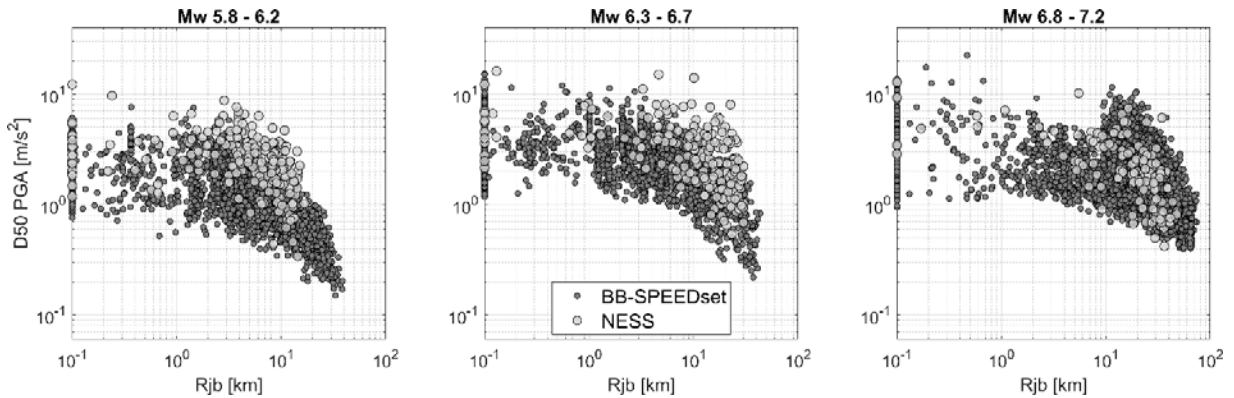
947

948 **Figure 7** SA(0.1s) and SA(5s) distribution from BB-SPEEDset (dark gray) in comparison with  
949 that from NESS (light gray) in the same range of magnitude. The D50 component is considered  
950 for both spectral accelerations.

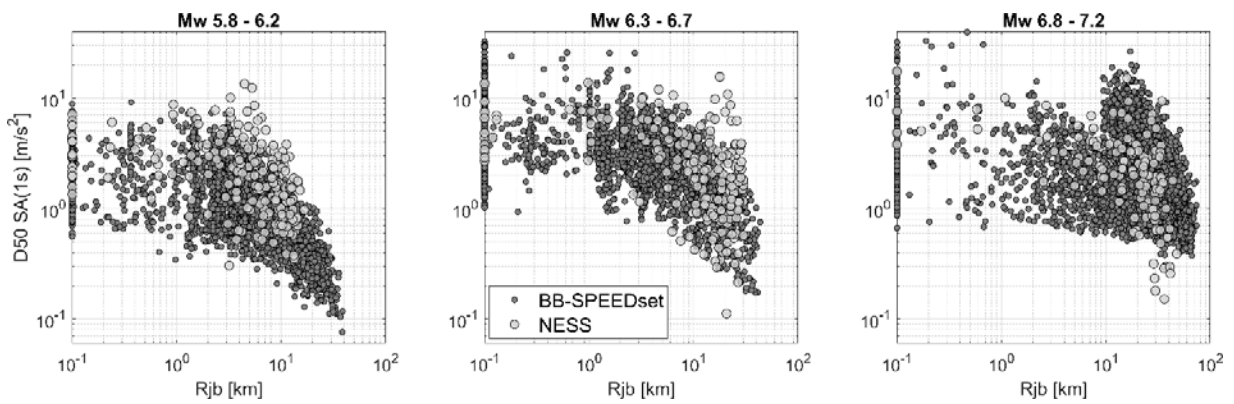
951

952

953

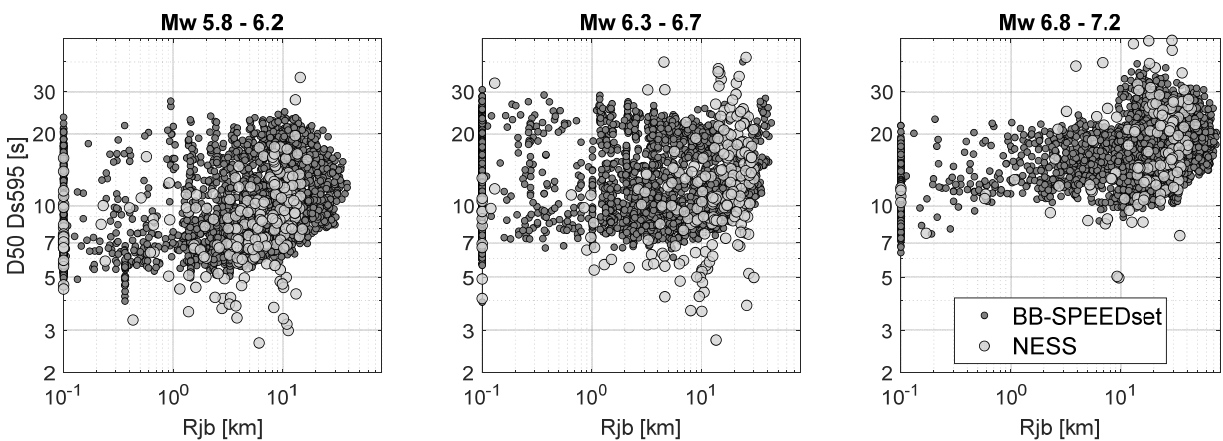


954  
955



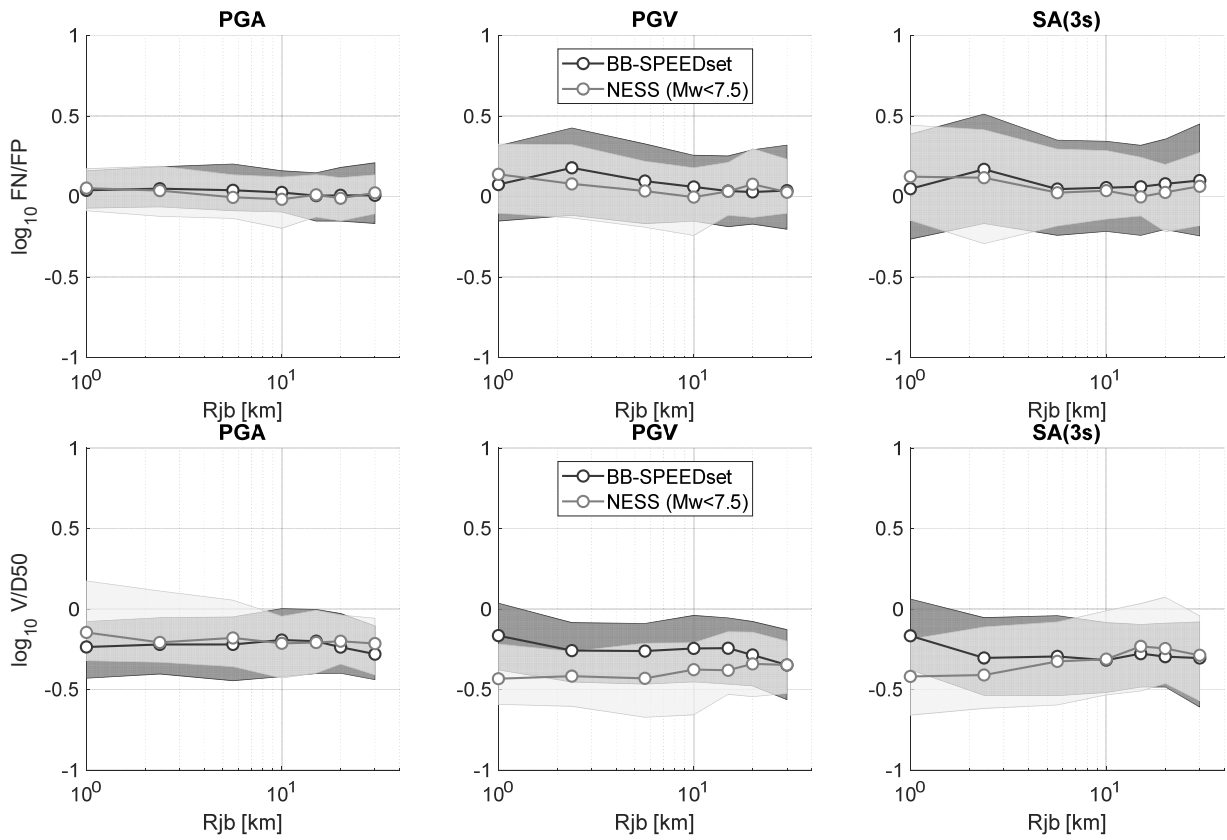
956  
957

958 **Figure 8** D50 components of PGA (top) and SA(1s) (bottom) as a function of  $R_{jb}$  distance, for  
 959 BB-SPEEDset (dark gray) and NESS (light gray), considering different  $M_w$  ranges (centered  
 960 around 6.0, 6.5 and 7.0).



961

962 **Figure 9** Duration  $D_{s595}$  (for D50 component) versus  $R_{jb}$  distance, for both BB-SPEEDset (dark  
 963 gray) and NESS (light gray), for different  $M_w$  ranges (centered around 6.0, 6.5 and 7.0).



964

965

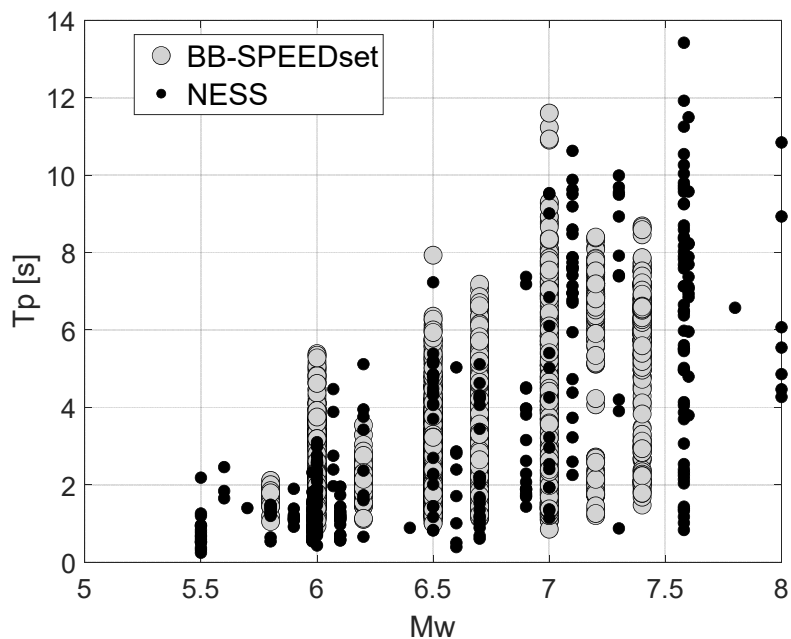
966 **Figure 10** Ratios of FN/FP (top) and of V/D50 (bottom) for PGA (left), PGV (center) and SA(3s)

967 (right), as a function of R<sub>jb</sub>. The median ±σ ratios from BB-SPEEDset (dark grey) and NESS (light

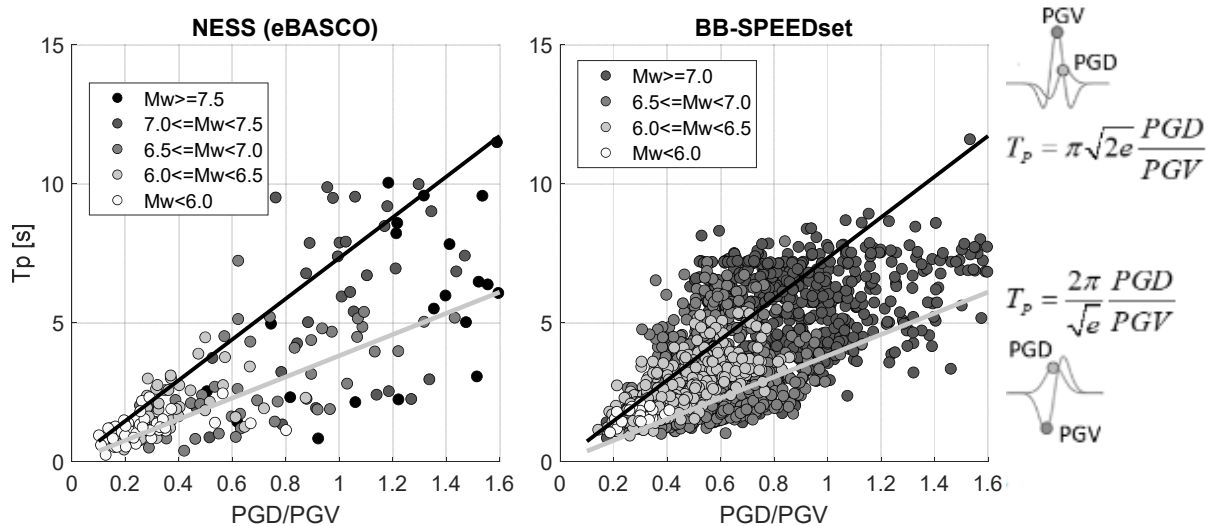
968 grey) are compared.

969

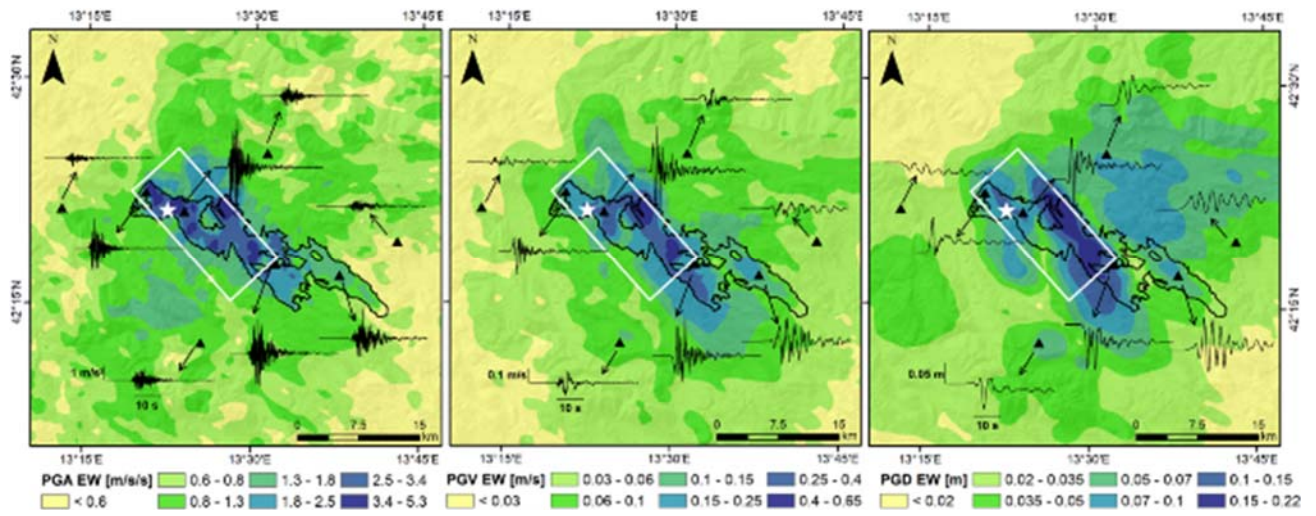
970



971  
 972 **Figure 11** Pulse period  $T_p$  versus earthquake magnitude for observed pulse-like ground motions  
 973 of BB-SPEEDset (20% of set data, in light gray) and NESS dataset (almost 30% of whole set data,  
 974 in black).



975  
 976 **Figure 12** Pulse period  $T_p$  as a function of PGD/PGV for the BB-SPEEDset dataset (right) and for  
 977 the NESS dataset (left), for different magnitude ranges, together with analytical relationships for  
 978 Ricker wavelet and double-impulse functions.



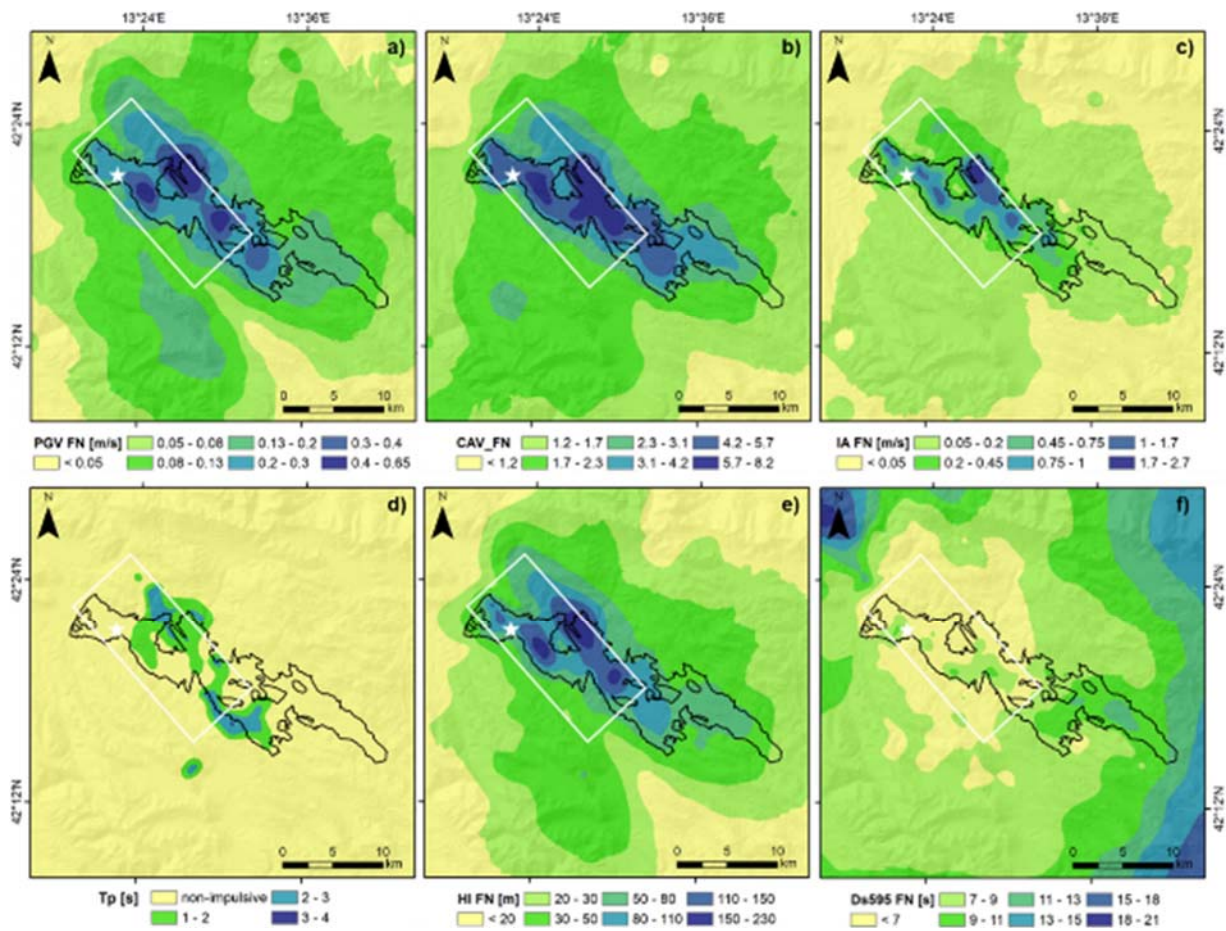
979

980 **Figure 13** Mw 6.2 L'Aquila 2009: peak ground motion maps (left: PGA; center: PGV; right: PGD)

981 and selected broadband waveforms (left: acceleration; center: velocity; right: displacement), EW

982 component, from BB-SPEEDset.

983



984

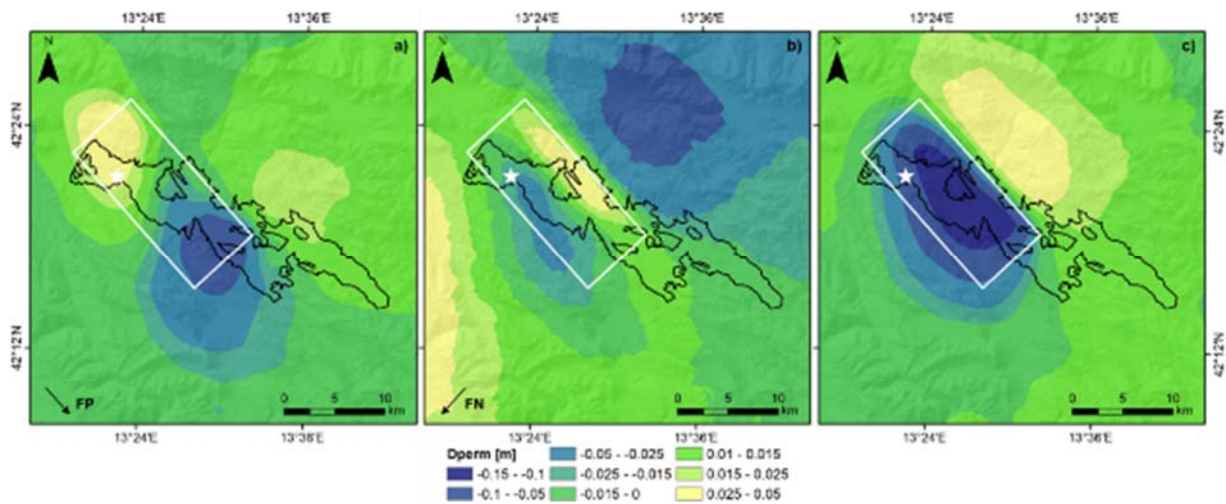
985 **Figure 14**  $M_w$  6.2 L'Aquila 2009: maps of different ground motion IMs stored in BB-SPEEDset,

986 a) PGV; b) Cumulative Absolute Velocity (CAV); c) Arias Intensity (IA); d) pulse period ( $T_p$ ); e)

987 Housner Intensity (HI); f) Duration between 5% and 95% of total IA (Ds595). For all IMs, except

988  $T_p$ , the FN component is shown.

989



990

991 **Figure 15**  $M_w$  6.2 L'Aquila 2009: maps of permanent displacement ( $D_{perm}$ ) on the three  
 992 components of motion, a) FP; b) FN; c) UD.

993

994